# Feature-consistent field inversion and machine learning framework with regularized ensemble Kalman method for improving the $k$-$\omega$ shear stress transport model in simulating separated flows

Long Chen and Yan Wang[*]

*State Key Laboratory of Mechanics and Control for Aerospace Structures and College of Aerospace Engineering, Nanjing University of Aeronautics and Astronautics, Yudao Street 29, Nanjing, Jiangsu 210016, China*

(Received 26 September 2024; accepted 10 January 2025; published 12 February 2025)

This work presents a feature-consistent field inversion and machine learning framework to enhance the capability of the Reynolds-averaged Navier-Stokes (RANS) turbulence model in predicting complex flows with separations. It effectively assimilates direct numerical simulation solutions and sparse experimental data, including velocity profiles, pressure distribution, and aerodynamic forces, into the improved $k$-$\omega$ shear stress transport (SST) closure model using the regularized ensemble Kalman inversion method. An artificial neural network (ANN) model is built to reconstruct the destruction term by considering local flow features. A modified analytical scheme with a prior mean-based regularization constraint is used to facilitate the model's exploration of the most influential regions for correction. The training process of the ANN model not only integrates the solution of the RANS equations but also minimizes the loss function by considering multiple flow conditions simultaneously so that feature inconsistency is avoided, resulting in a more effective model that delivers more accurate RANS results. Typical turbulent flow problems are simulated to validate the proposed method, including the separation flows over slopes and steps with low Reynolds numbers and the separation flows over airfoils with high Reynolds numbers. It is demonstrated that the proposed framework is capable of training a robust and consistent ANN-improved $k$-$\omega$ SST turbulence model for predicting turbulent flows with separations at both low and high Reynolds numbers. It also shows that the present ANN-improved $k$-$\omega$ SST turbulence model achieves generalization for separated flows with unforeseen geometries and Reynolds numbers.

DOI: 10.1103/PhysRevFluids.10.024603

## I. INTRODUCTION

Turbulence is a kind of ubiquitous flow phenomenon in natural and engineered systems. Precise simulations of turbulent flows are paramount for the practical applications of computational fluid dynamics (CFD). It is still challenging, however, to efficiently solve engineering problems through direct numerical simulation (DNS) or large eddy simulation (LES) due to the prohibitively high computational costs. Despite their superior computational accuracy, it is unlikely that these limitations will be resolved in the next few decades [1]. In contrast, the efficient and robust Reynolds-averaged Navier-Stokes (RANS) equations with linear eddy viscosity models (LEVMs), such as the most widely used $k$-$\omega$ shear stress transport (SST) model, $k$-$\varepsilon$, and Spalart-Allmaras (SA) turbulence closures [2–4], are still the workhorse for turbulence modeling in the industry.

[*]Contact author: aerowangy@nuaa.edu.cn

 

Traditionally, during their initial development, the closure models were optimized for simplified test flows and introduced certain assumptions, inevitably leading to errors and uncertainties for complex turbulence. As a result, the RANS models often struggle to predict separated flows accurately [5]. These disadvantages underscore the importance of developing a high-precision RANS turbulence model without losing robustness and efficiency.

In recent years, the introduction of modern machine learning (ML) methods provides a modular and agile modeling framework that can be tailored to address many challenges in fluid mechanics [6]. For turbulence closure modeling, ML techniques have offered a promising opportunity to integrate insights from readily available high-fidelity data and experiments into RANS simulations, leading to enhanced predictions. This new paradigm has gained significant traction. In boundary layer separation flows caused by an adverse pressure gradient, the Reynolds stress level within the boundary layer largely determines its ability to resist the gradient and the characteristics of the separated flow. Therefore, the solution of Reynolds stress in turbulence models impacts the simulation accuracy of separation flows. The modeling of the Reynolds stress constitutive relation and the eddy viscosity coefficient are two breakthroughs. Up to now, the turbulence modeling approaches can be classified into two categories: direct modeling and assimilation modeling.

The direct modeling method utilizes abundant high-fidelity flow field data to train the closure terms of the RANS equations, with the training targets being the Reynolds stress or the eddy viscosity coefficient. Ling *et al.* [7] pioneered the development of a novel tensor basis neural network (TBNN) architecture for modeling the anisotropic Reynolds stress tensor based on the tensor representation theory proposed by Pope [8], which addressed the issue of the commonly used LEVM being incapable of predicting complex flows. This concept, resembling that of a nonlinear eddy viscosity model, inspired subsequent studies. For instance, Geneva and Zabaras [9] employed the Bayesian deep learning framework for Reynolds stress modeling to enhance the RANS simulations, enabling the quantification of model form uncertainty present in turbulence modeling. Furthermore, owing to the opaque nature of traditional machine learning, numerous interpretable data-driven techniques, including gene expression programming (GEP), sparse regression, symbolic regression, etc. [10–12], have been employed to model explicit Reynolds stress. For the eddy viscosity coefficient modeling, Zhu *et al.* [13] constructed a neural network model coupled bidirectionally with the solver, using the eddy viscosity coefficient of the SA model as the training target. This method achieves wall friction and pressure comparable to the accuracy of the SA model. Additionally, Liu *et al.* [14] developed eddy viscosity modeling for large separated flows and analyzed the coupling stability.

However, due to the lack of high-fidelity flow field data, direct modeling methods may not be suitable for high Reynolds numbers or complex geometry flows. Data assimilation modeling methods address this challenge effectively by combining sparse experimental data with data assimilation (DA) techniques to correct or construct turbulence closure terms. The DA methods are widely used in the posterior inference of closure terms' uncertainty correction parameters. Assuming that the prior distribution of the uncertainty parameters is known, such research aims to compute the posterior distribution given observation data $Y$. This is essentially a Bayesian inference problem: Singh and Duraisamy [15] multiplied a spatial correction field $\beta(x)$ with the production term $P(\tilde{\nu}, U)$ of the SA model as $\frac{D\tilde{\nu}}{Dt} = \beta(x)P(\tilde{\nu}, U) - D(\tilde{\nu}, U) + T(\tilde{\nu}, U)$; the posterior distribution of the correction field $\beta(x)$ is optimized by minimizing the discrepancies between the solver results and sparse observations of DNS or experiment. During the optimization process, the adjoint method [16] calculates the gradients. Furthermore, Singh *et al.* [17] proposed a field inversion and machine learning (FIML) framework, which adopted machine learning technology to construct the relationship between the local dimensionless mean flow and the correction field $\beta(x)$. They utilized this framework to augment the SA model for separated flow over the airfoil and demonstrated that the enhanced SA model exhibits commendable generalization and convergence properties. Subsequently, the FIML framework, with the adjoint method, was extensively employed for turbulence model correction. For instance, Yan *et al.* [18] applied this framework to modify the SA model and incorporate additional nonlinear terms for modeling three-dimensional separation flows. Wu and Zhang [19] substituted the traditional machine learning approach within the FIML framework with a symbolic regression model to enhance the interpretability of the improved RANS model. Furthermore, even when applying the improved turbulence model to the laminar flow over a flat plate, it still maintains accuracy comparable to the baseline turbulence model. Unfortunately, the adjoint method requires solving the derivative of the cost function with respect to the optimization variable using the solver. Due to its invasive nature, the inversion of different flow problems using this method necessitates significant code modification and substantial computational resources, posing challenges to its widespread applicability.

Given these difficulties, motivated by the classic ensemble Kalman filter (EnKF) [20] method initially proposed by Evensen for the data assimilation in nonlinear problems, Iglesias *et al.* [21] introduced an iterative ensemble Kalman method, called ensemble Kalman inversion (EKI), which is particularly suitable for field inversion in various CFD problems due to its derivative-free nature. Additionally, Zhang *et al.* [22] demonstrated that the EKI method converges faster than the adjoint method for the same inverse problem. However, the traditional EKI method may lead to ill-posed inferences due to its inability to incorporate regularization terms in the cost function. To address this inherently ill-posed problem, Iglesias [23] introduced the regularization based on the Levenberg-Marquardt (LM) [24] scheme into the original iterative EnKF method, and Luo *et al.* [25] demonstrated that the LM-based iterative ensemble method performs well in solving the minimum-average-cost (MAC) problem, particularly in strongly nonlinear systems. Zhang *et al.* [26] proposed a novel regularized ensemble Kalman inversion (REKI) method with a modified analysis scheme that implicitly minimizes a cost function with generalized constraints. Building upon these, Yang and Xiao [27] employed the FIML framework with the REKI method to modify the $k$-$\omega$-$\gamma$-$A_r$ transition model for low-speed transitional flows. Similarly, Zhang *et al.* [28] enhanced the four-equation $\gamma$-$\mathrm{Re}_\theta$ transition model in the hypersonic boundary layer using this framework.

Despite the improved performance presented in the works above, these methods employ offline training, meaning that the model training and solver predictions are separate. These separate steps introduce the opportunity for inconsistency. Wu *et al.* [29] have shown that minor errors in the machine learning model can rapidly amplify in the RANS solver. Moreover, Liu *et al.* [14] confirmed that the error amplification caused by inconsistency is more severe in high Reynolds number separated flows. While some studies [12,29,30] have demonstrated that implicitly handling data-driven Reynolds stress models can effectively alleviate this problem, applying these methods in high Reynolds number cases is challenging due to the scarcity of high-fidelity data. Similarly, the classic FIML framework for baseline turbulence model correction adopts offline learning separate from the inversion, resulting in an inconsistency between the inversion and the prediction environment. Therefore, researchers have adopted a method of directly inverting model parameters to integrate inversion and training into one step, ensuring the posterior accuracy of model coupling. Zhao *et al.* [31] used the GEP model with sparse high-fidelity LES data to construct a nonlinear Reynolds stress closure term. Zhang *et al.* [22] employed the EnKF method with TBNN for nonlinear Reynolds stress modeling in secondary and separated flow. On this basis, Wang and Zhang [32] used the EnKF method to perform transfer learning and built an eddy viscosity model. Aulakh *et al.* [33] calibrated the coefficients of the SA turbulence model with EnKF. In particular, they artificially defined the sensitive coefficient $C_{b1}$ as an expressions related to the dimensionless characteristics of local flows to improve model performance.

In light of the above studies, this paper presents an improved FIML framework based on REKI for improving the $k$-$\omega$ SST turbulence model, emphasizing consistency and regularization. First, unlike the classic FIML framework, the improved FIML framework ensures consistency between the inversion and prediction environments by integrating field inversion and machine learning. Specifically, the improved FIML framework incorporates prediction information in observation space from the solver during the model training process to guide the optimization of parameters, addressing the issue of inconsistency in traditional methods. The ANN is applied to correct the destruction term in the $\omega$'s transport equation, and the parameters of the ANN are optimized using the REKI method. It is worth noting that, although many terms of the turbulence model have uncertainties, the eddy viscosity coefficient is not unique. Thus, we can still align the solver results with the experimental data by adjusting only the destructive terms to modify the eddy viscosity coefficient in the areas of interest. In addition, this work applies the REKI method with a modified analysis scheme to optimize the ANN's parameters. An additional constraint on the spatial correction field $\beta$ is added to the cost function. Including regularization terms facilitates the exploration of regions in the inversion process that are more sensitive to model corrections, aiming to achieve inversion optimization by minimizing the correction area and magnitude as much as possible.

The remainder of this paper is organized as follows. Section II introduces the incompressible governing equations of the solver, the form of the ANN-improved $k$-$\omega$ SST turbulence model, and the inversion method utilized in the improved FIML framework. In Sec. III, the improved framework is applied to the low Reynolds number and high Reynolds number separation flow cases to verify the robustness and generalizability of the ANN-improved $k$-$\omega$ SST turbulence model. Finally, a summary of the contribution is demonstrated in Sec. III.

## II. METHODOLOGY

### A. Governing equations

The SimpleFoam solver in the open-source CFD platform OpenFOAM [34] is utilized to solve the two-dimensional incompressible turbulent flow. The governing RANS equations read

$$\nabla \cdot \boldsymbol{u} = 0. \tag{1}$$

$$\frac{\partial \boldsymbol{u}}{\partial t} + \boldsymbol{u} \cdot \nabla \boldsymbol{u} = -\nabla p + \nu \nabla^2 \boldsymbol{u} - \nabla \cdot \boldsymbol{\tau}, \tag{2}$$

where $\boldsymbol{u}$, $p$, and $\nu$ are the mean velocity, mean pressure (normalized by density), and viscosity, respectively. $\boldsymbol{\tau}$ is the Reynolds stress accounting for unresolved turbulence:

$$\boldsymbol{\tau} = \tfrac{2}{3} k \boldsymbol{I} - \upsilon_t [\nabla \boldsymbol{u} + (\nabla \boldsymbol{u})^T]. \tag{3}$$

Herein, the Reynolds stress is unknown and needs to be closed by a mathematical model. It is generally recognized that the turbulence closure model is the most critical factor in the prediction accuracy of RANS equations, in addition to the effects regarding the discretization schemes and numerical algorithms.

### B. ANN-improved *k*-*ω* SST turbulence model

The $k$-$\omega$ SST turbulence model [2] effectively combines the robustness and accuracy of the $k$-$\omega$ model in the near-wall region with the $k$-$\varepsilon$ model's advantages in computing the far-field flow independent of the free stream. It incorporates an additional term for the transverse dissipation derivative and considers the transport process of turbulent shear stress. The specific form of the model is as follows:

$$\begin{aligned}
&\frac{\partial k}{\partial t} + \boldsymbol{u} \cdot \nabla k = P_k - \beta^* \rho \omega k + \nabla \cdot (\nu_{\mathrm{eff},k} \nabla k), \\
&\frac{\partial \omega}{\partial t} + \boldsymbol{u} \cdot \nabla \omega = \frac{\delta}{\nu_t} P_k - \theta \rho \omega^2 + \nabla \cdot (\nu_{\mathrm{eff},\omega} \nabla \omega) + 2(1 - F_1) \frac{\rho \sigma_{\omega 2}}{\omega} \nabla k : \nabla \omega.
\end{aligned} \tag{4}$$

In the equation,

$$\nu_{\mathrm{eff},k} = \nu + \sigma_k \nu_t, \quad \nu_{\mathrm{eff},\omega} = \nu + \sigma_\omega \nu_t, \quad P_k = -\boldsymbol{\tau} : \nabla \boldsymbol{u},$$

$$F_1 = \tanh\left(\arg_1^4\right), \quad \arg_1 = \min\left[\max\left(\frac{\sqrt{k}}{\beta^* \omega d}, \frac{500\nu}{d^2\omega}\right), \frac{4\sigma_{\omega 2} k}{CD_{k\omega} d^2}\right],$$

$$CD_{k\omega} = \max\left(2\frac{\sigma_{\omega 2}}{\omega}\nabla k : \nabla\omega, 10^{-20}\right), \tag{5}$$

where $\nu$ denotes the dynamic viscosity, $\nu_t$ the eddy viscosity, and $d$ the wall distance. Further introduction of a turbulence viscosity limitation makes it more widely applicable:

$$\nu_t = \frac{k}{\omega}\left(1/\max\left[1, \frac{SF_2}{0.31\omega}\right]\right),$$

$$F_2 = \tanh\left(\left(\max\left[\frac{2\sqrt{k}}{0.09\omega d}, \frac{500\nu}{d^2\omega}\right]\right)^2\right). \tag{6}$$

The model coefficients $\beta^*$, $\sigma_k$, $\sigma_{\mathrm{w}}$, $\delta$, and $\theta$ in Eq. (4) are calculated by the blend function $F_1$ and can be expressed as

$$\phi = F_1\phi_1 + (1 - F_1)\phi_2,$$

$$\phi = [\beta^*, \sigma_k, \sigma_\omega, \delta, \theta],$$

$$\phi_1 = [\beta_1^*, \sigma_{k1}, \sigma_{\omega 1}, \delta_1, \theta_1],$$

$$\phi_2 = [\beta_2^*, \sigma_{k2}, \sigma_{\omega 2}, \delta_2, \theta_2], \tag{7}$$

where $\phi_1$ denotes the $k$-$\omega$ model's coefficients and $\phi_2$ denotes the $k$-$\varepsilon$ model's coefficients. In this work, the standard values are adopted [2]. It is important to emphasize that the constant coefficients used in the standard $k$-$\omega$ SST turbulence model are calibrated based on simplified theories and limited experimental data. As a result, the accuracy of the baseline $k$-$\omega$ SST model may be compromised when simulating complex turbulent flows.

Several researchers have proposed various modifications to make the $k$-$\omega$ SST model sensitive to rotation and streamline curvature to address this issue. These methods primarily involve changes to the turbulent length scale or adjustments to the damping term in the dissipation equation. Smirnov and Menter [35] extended the RC correction method developed by Spalart and Shur to the $k$-$\omega$ SST model, resulting in the RC-corrected $k$-$\omega$ SST model, also referred to as the SST-CC model. Dhakal and Walters [36] modified the $k$-$\omega$ SST turbulence model by considering the effects of rotation and streamline curvature based on the mean flow velocity gradient, leading to the SST $k$-$\omega$-$v^2$ model. This model introduces an additional transverse turbulent velocity scale, represented by the $v^2$ transport equation, which carries information about the turbulent structures induced by rotation and streamline curvature. Moreover, Hellsten [37] replaced the turbulent timescale used in the RI expression with the average flow timescale. Then, the destruction term of the $\omega$ transport equation of the $k$-$\omega$ SST turbulence model is corrected to obtain the $k$-$\omega$ RCSST model. Considering rotation and curvature while avoiding the complexity of the above RC correction, e.g., second-order velocity derivatives.

This issue can be effectively addressed in this work by utilizing the developed ANN-improved $k$-$\omega$ SST turbulence model. In this study, the baseline turbulence model's prediction error primarily arises from inaccuracies in predicting the shear layer within the separation bubble caused by a strong reverse pressure gradient. Identifying this flow structure is crucial for improving the accuracy of the turbulence model. Additionally, the relative size ratio of turbulence-related physical quantities can be used to gauge the extent to which the benchmark model accurately identifies the flow structure. By incorporating these input features, the model can better pinpoint the errors in the reference turbulence model and provide a corrective direction. Considering these factors, six local scalar

TABLE I. Input feature set.

| Feature | Description | Formula | Note |
|---|---|---|---|
| $\eta_1$ | Vortex Reynolds number (rotation) | $\|\|\mathbf{\Omega}\|\|d^2/(\nu+\nu_t)$ | $\mathbf{\Omega}=\frac{1}{2}[\nabla\boldsymbol{u}-(\nabla\boldsymbol{u})^T]$ |
| $\eta_2$ | Vortex Reynolds number (strain) | $\|\|\mathbf{S}\|\|d^2/(\nu+\nu_t)$ | $\mathbf{S}=\frac{1}{2}[\nabla\boldsymbol{u}+(\nabla\boldsymbol{u})^T]$ |
| $\eta_3$ | Normalized mean rotation rate | $\|\|\mathbf{\Omega}\|\|/(\|\|\mathbf{\Omega}\|\|+\|\|\mathbf{S}\|\|)$ | |
| $\eta_4$ | Turbulence intensity | $k/(k+0.5\|\boldsymbol{u}\|^2)$ | |
| $\eta_5$ | Scalar function 1 | $\mathrm{Tr}(\hat{\mathbf{S}}^2)$ | $\widehat{\mathbf{S}}=\mathbf{S}/(\|\|\mathbf{S}\|\|+\omega)$ |
| $\eta_6$ | Scalar function 2 | $\mathrm{Tr}(\hat{\mathbf{\Omega}}^2)$ | $\widehat{\mathbf{\Omega}}=\mathbf{\Omega}/(\|\|\mathbf{\Omega}\|\|+\omega)$ |

features are selected in Table I, where $\boldsymbol{u}$ denotes the mean velocity, $k$ the turbulent kinetic energy, $\mathbf{S}$ the mean strain rate, $\mathbf{\Omega}$ the mean rotation rate, $\widehat{\mathbf{S}}$ the local dimensionless form of $\mathbf{S}$, $\widehat{\mathbf{\Omega}}$ the local dimensionless form of $\mathbf{\Omega}$,$\mathrm{Tr}(\bullet)$the trace, $|\bullet|$ the vector norm, and $||\bullet||$ the Frobenius matrix norm.

The first two features are the vortex Reynolds numbers, which help identify flow shear layers and vortex flows. Singh *et al.* [17] utilized the feature $\eta_1$ to correct the generation term of the SA model. The third feature is the normalized mean rotation rate, similar to the Q criterion [38], which aids in identifying the vortex. The fourth feature is the turbulence intensity, which provides information about the level of turbulence present in the flow. The last two features are based on the stress tensor decomposition theory proposed by Pope [8]. Only these two scalar independent invariants are nonzero for statistically two-dimensional flows, making them valuable in identifying flow characteristics. By extracting the flow-field input features for each grid point, the ANN model can be expressed as

$$\beta(\boldsymbol{\eta})=1+f(w,b,\widehat{\eta}_1,\ldots,\widehat{\eta}_n),\quad \boldsymbol{\eta}=[\widehat{\eta}_1,\widehat{\eta}_2,\ldots,\widehat{\eta}_n], \tag{8}$$

where $f$ represents the ANN model, $\widehat{\eta}_{\mathrm{n}}$ is the normalized input feature, and $w$ and $b$ are the weights and biases of the ANN, respectively; subsequently, following the correction strategies adopted in Ref. [19], the correction field $\beta(\boldsymbol{\eta})$ is used to multiply the $\omega$-destruction term. It is worth noting that, despite potential uncertainties in other terms of the model, modifying only the $\omega$-destruction term effectively controls the magnitude of turbulent shear stress, thereby improving the predictive capability of the SST model. From both the equation and physical perspectives, larger $\beta$ leads to stronger destruction of $\omega$ and weaker dissipation of $k$ [$\beta^*\rho\omega k$ in Eq. (4)], resulting in a smaller $\omega$ and a larger $k$. This increases the eddy viscosity coefficient, which in turn leads to increased momentum exchange, making the predicted separation bubble smaller, while smaller $\beta$ leads to a larger separation vortex. Moreover, changing only one parameter less impacts other flows and increases computational stability. Based on these considerations, we have performed the inverse correction only on the $\omega$-destruction term. The corrected turbulent transport equation can be expressed as follows:

$$\frac{\partial\omega}{\partial t}+\boldsymbol{u}\cdot\nabla\omega=\frac{\gamma}{\nu_t}P_k-\beta(\boldsymbol{\eta})\theta\rho\omega^2+\nabla\cdot(\nu_{\mathrm{eff},\omega}\nabla\omega)+2(1-F_1)\frac{\rho\sigma_{\omega 2}}{\omega}\nabla k:\nabla\omega. \tag{9}$$

ANNs are essential tools in machine learning that have drawn increasing attention to flow modeling [39–42]. Figure 1 shows a neural network structure with $n$ inputs and one output. The traditional learning mechanism of an ANN encompasses two principal phases: forward propagation and backward propagation. During forward propagation, the input data progress from the input layer through the hidden layers to the output layer, with each neuron calculating a weighted sum and applying an activation function to produce an output signal. Backward propagation involves adjusting the network's weights by backward-propagating the loss function using the gradient descent algorithm to minimize errors and refine the model's predictions.

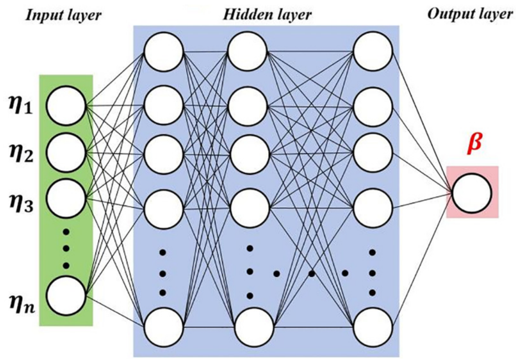


FIG. 1. Sketch of the artificial neural network.

With high efficiency and superior nonlinear fitting capabilities, the ANN model is employed to enhance the baseline turbulence model by modeling the nonlinear relationships between local dimensionless features and the correction field. This work employs backward propagation in the pretraining phase to establish a set of initial parameters, as detailed in the next section. The derivative-free REKI method is utilized for the subsequent training to optimize the parameters. The implementation of the ANN is carried out using TensorFlow, and the coupling between the trained ANN model and the solver is completed using the application programming interface (API) [43]. Next, we will discuss optimizing the ANN model's parameters to minimize the discrepancy between the predicted mean flow from the improved turbulence model and the reference mean flow.

### C. REKI method for data assimilation and parameter optimization

Data assimilation (DA) is a powerful technique that enhances the predictive capabilities of numerical models by integrating observational data. By combining information from diverse sources, DA creates a more accurate link between simulations and observations. This approach finds widespread application in weather forecasting, ocean modeling, and environmental science [44,45]. A notable DA method is the EnKF [20], a derivative-free estimation technique. The EnKF employs a collection of random samples to represent the model state's probability distribution, updating these samples to incorporate new observational data effectively. Iglesias *et al.* [21] further developed an iterative EnKF method for the inversion problem and demonstrated that the EnKF method provides comparable accuracy to the traditional least-squares approaches. On this basis, Kovachki and Stuart [46] attempted to use the EKI method instead of stochastic gradient descent (SGD) to optimize the parameters of machine learning models. Luo [47] confirmed the reasonable performance of the ensemble-based learning method in supervised learning problems (SLPs) and further extended this idea to the DA problem involving forward simulators with errors. These works embrace this approach by employing the REKI method to invert the parameters of the ANN that represent correction coefficients $\beta$, thereby ensuring the posterior accuracy of the ANN model embedded within the solver. Briefly, the parameters of the ANN model serve as the adjustable parameters, and the primary optimization objective in the observation space is to minimize the discrepancy between the convergence result of the ANN-embedded RANS solver and the reference value. Based on Bayesian theory and the Gaussian distribution assumption,

$$p(\boldsymbol{\chi}|\boldsymbol{y}) \propto p(\boldsymbol{\chi})p(\boldsymbol{y}|\boldsymbol{\xi}(\boldsymbol{\chi})) \propto \exp\left(-||\boldsymbol{\chi}-\boldsymbol{\chi}^f||^2_{\mathbf{P}^{-1}} - ||\boldsymbol{y}-\boldsymbol{\xi}(\boldsymbol{\chi}^f)||^2_{\boldsymbol{\Gamma}^{-1}}\right), \tag{10}$$

where the operator $\| \boldsymbol{A} \|^2_{B^{-1}}$ is defined as $\boldsymbol{A}^T\boldsymbol{B}\boldsymbol{A}$; $\boldsymbol{\chi}$ denotes the uncertain quantity (the weights $w$ and biases $b$ of the ANN model in this paper, which can be expressed as $\boldsymbol{\chi} = [w, b]$), $\boldsymbol{y}$ the high-fidelity observations obtained from experiments or numerical simulations, $\boldsymbol{\xi}(\bullet)$ the propagation process that maps the state space into the observation space using the solver, and $\mathbf{P}$ the covariance matrix of the uncertain quantity. $\mathbf{\Gamma}$ is the covariance of the observation error, $p(\boldsymbol{\chi})$ is the prior distribution of the uncertain quantity $\boldsymbol{\chi}$, and $p(\boldsymbol{y}|\xi(\boldsymbol{\chi}))$ is the likelihood probability distribution between predictions and observations. Maximizing the posterior probability is equivalent to minimizing the loss function as follows:

$$\mathscr{J}(\boldsymbol{\chi})= ||\boldsymbol{\chi} - \boldsymbol{\chi}^f||^2_{\mathbf{P}^{-1}} + ||\boldsymbol{y} - \boldsymbol{\xi}(\boldsymbol{\chi})||^2_{\mathbf{\Gamma}^{-1}}. \tag{11}$$

Moreover, by incorporating an additional custom regularization term about prior mean values to limit the search space of the optimal solution, articulate the final loss function as

$$\mathscr{J}(\boldsymbol{\chi})=||\boldsymbol{\chi} - \boldsymbol{\chi}^f||^2_{\mathbf{P}^{-1}} + ||\boldsymbol{y} - \boldsymbol{\xi}(\boldsymbol{\chi})||^2_{\mathbf{\Gamma}^{-1}} + ||\beta - 1||^2_{\mathbf{Q}^{-1}}. \tag{12}$$

The covariance of the observation error $\Gamma$ represents the weights of different observation points, with smaller weights indicating the lower importance of that observation point in the inversion process. In this work, adaptively adjusting the observation weights based on ensemble observation space information to accelerate the convergence of the inversion algorithm, $\mathbf{Q}$ is the weighting matrix for the regularization term.

The initial ensemble samples are critical for the inversion process because random initial parameters can lead to abnormal model outputs, resulting in solver divergence. To prevent this, the ANN model should be pretrained and embedded into the solver to achieve performance comparable to the baseline model. This pretraining process can be expressed as

$$\beta(\boldsymbol{\eta}) = 1+\boldsymbol{f}(w^0,b^0,\widehat{\eta}_1,\widehat{\eta}_2,\ldots,\widehat{\eta}_n) = 1. \tag{13}$$

The initial ensemble $\boldsymbol{\chi} = \mathrm{span}\{\chi_0^m\}_{m=1}^M$ satisfies a Gaussian process:

$$\boldsymbol{\chi} \sim \mathrm{N}([w^0, b^0], \kappa), \tag{14}$$

where $w^0$ and $b^0$ represent the initial weight and bias of the ANN model. Then, the REKI algorithm is primarily divided into a prediction step and an analysis step. In the prediction step, the ensemble of the current uncertain input state (the parameters of the neural network) is mapped into the observation space, thereby incorporating information about the forward model (RANS solver). The analysis step compares the mapped ensemble in the observation space with the observational high-fidelity data, adjusting the ensemble to better align with the observational data. This paper utilizes the open-source data assimilation and field inversion (dafi) framework developed by Ströfer *et al.* [48] to perform inversion corrections on the ANN-improved SST turbulence model. The specific steps are as follows:

(1) Prediction step: Embed the correction field corresponding to each sample into the RANS solver for propagation. After convergence, extract the corresponding observations $\gamma_m^n = \xi(\chi_m^n)$, where $m$ represents the sample index, and $n$ is the iteration step. Compute the sample mean accordingly:

$$\overline{\gamma}^n = \frac{1}{M}\sum_{m=1}^{M}\gamma_m^n, \overline{\chi}^n = \frac{1}{M}\sum_{m=1}^{M}\chi_m^n. \tag{15}$$

(2) Analysis step: Introduce a linear operator as an estimate that satisfies $\boldsymbol{\xi}(\boldsymbol{\chi}) = \mathbf{E}\boldsymbol{\chi},\ \boldsymbol{\xi}'(\boldsymbol{\chi}) = \mathbf{E}$. According to Ref. [26], the updated format for the parameters is

$$\chi_m^{n+1} = \chi_m^n + \mathbf{K}\big(y_m - \mathbf{E}\chi_m^n\big) + \boldsymbol{\delta}. \tag{16}$$

In the equation, $\mathbf{K}$ is the Kalman gain matrix, and $\boldsymbol{\delta}$ is the additional correction generated by the regularization term. The specific form is given by the following equations:

$$\mathbf{K} = \mathbf{P}\mathbf{E}^T(\mathbf{E}\mathbf{P}\mathbf{E}^T + \boldsymbol{\Gamma})^{-1}, \tag{17}$$

$$\boldsymbol{\delta} = -\frac{\lambda_n}{||\mathbf{P}||_F}\mathbf{P}\mathcal{G}'(\boldsymbol{\chi}^n)^T\mathbf{W}\mathcal{G}(\boldsymbol{\chi}^n), \tag{18}$$

$$\lambda_n = 0.5\lambda_0\left[\tanh\left(\frac{n-s}{d}\right)+1\right], \tag{19}$$

where $\mathbf{P} = \mathbf{C}_\chi\mathbf{C}_\chi^T$, and $\mathcal{G}(\bullet)$ represents the regularization term; the change law of the regular term with the iteration step can be adjusted by changing $s$ and $d$ in the ramp function. $\mathbf{W}$ is taken as the identity matrix $\boldsymbol{I}^{J\times J}$ in this paper, and $J$ is the number of grid points. Since the above update format cannot be directly implemented in the program, the Kalman gain matrix $\mathbf{K}$ is further simplified as follows:

$$\begin{aligned}
\mathbf{K} &= \mathbf{P}\mathbf{E}^T(\mathbf{E}\mathbf{P}\mathbf{E}^T + \boldsymbol{\Gamma})^{-1} \\
&= \mathbf{C}_\chi\mathbf{C}_\chi^T\mathbf{E}^T\left(\mathbf{E}\mathbf{C}_\chi\mathbf{C}_\chi^T\mathbf{E}^T + \boldsymbol{\Gamma}\right)^{-1} \\
&= \mathbf{C}_\chi(\mathbf{E}\mathbf{C}_\chi)^T(\mathbf{E}\mathbf{C}_\chi(\mathbf{E}\mathbf{C}_\chi)^T + \boldsymbol{\Gamma})^{-1} \\
&= \mathbf{C}_\chi\mathbf{C}_\gamma^T\left(\mathbf{C}_\gamma\mathbf{C}_\gamma{}^T + \boldsymbol{\Gamma}\right)^{-1} \\
&= \mathbf{C}_{\chi\gamma}(\mathbf{C}_{\gamma\gamma} + \boldsymbol{\Gamma})^{-1}.
\end{aligned} \tag{20}$$

In the equation, the covariance matrix regarding the ensemble observations $\boldsymbol{\gamma}$ and the inversion parameters $\boldsymbol{\chi}$ is as follows:

$$\begin{aligned}
\mathbf{C}_{\chi\gamma} &= \frac{1}{M-1}\sum_{m=1}^{M}\left(\chi_m^n - \overline{\chi^n}\right)\left(\gamma_m^n - \overline{\gamma^n}\right)^T, \\
\mathbf{C}_{\gamma\gamma} &= \frac{1}{M-1}\sum_{m=1}^{M}\left(\gamma_m^n - \overline{\gamma^n}\right)\left(\gamma_m^n - \overline{\gamma^n}\right)^T.
\end{aligned} \tag{21}$$

(3) Check for convergence: Determine if the error or the number of iterations has reached a specified value. If so, consider the process to have converged; otherwise, return to step 2.

### D. Overall framework

In summary, the improved FIML framework for ANN-improved $k$-$\omega$ SST turbulence modeling based on REKI is constructed, as shown in Fig. 2. The overall training process can be broken down into the following steps:

(1) Select appropriate dimensionless mean features $\boldsymbol{\eta}$ as the input of the artificial neural network. Here, $\boldsymbol{\eta} = [\widehat{\eta}_1, \widehat{\eta}_2, \ldots, \widehat{\eta}_n]$.

(2) Calculate the mean flow field via the baseline $k$-$\omega$ SST turbulence model and obtain the initial ensemble of parameters by pretraining.

(3) Add the spatially varying field $\beta$ to correct the destruction term $\theta\rho\omega^2$ in the $\omega'$ transport equation of the $k$-$\omega$ SST turbulence model.

(4) Fine-tune and optimize the initial parameter samples through the REKI method, noting that the freezing assumption is used in this process, which means that the fixed correction field $\beta$ of the ANN's output is propagated through the RANS solver to obtain the results in observation space, which can be referred to as semicoupled.

(5) After REKI converges, calculate the average value of parameter samples and construct the final ANN model.

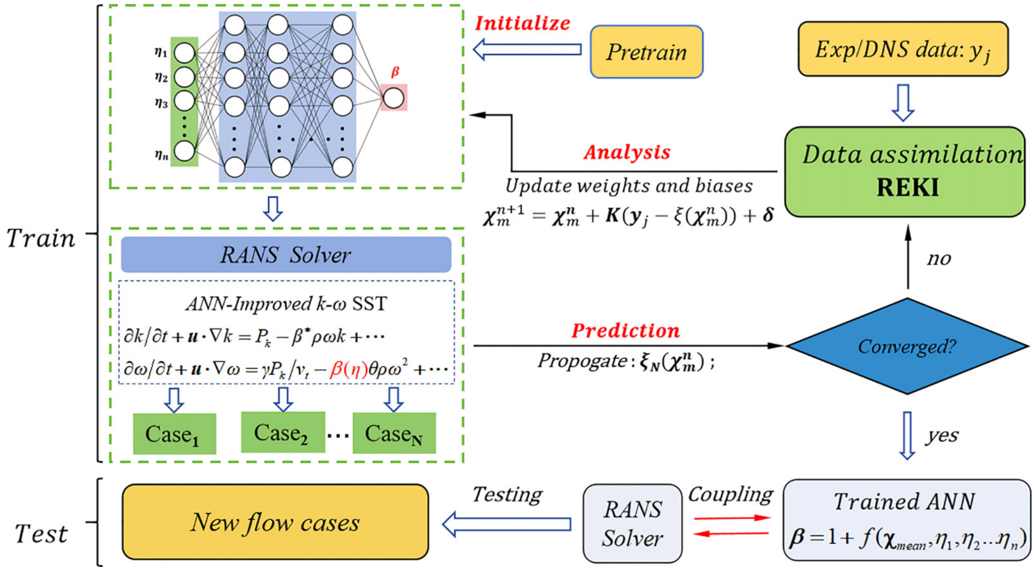


FIG. 2. Framework for ANN-improved $k$-$\omega$ SST turbulence modeling.

(6) Fully couple the RANS solver and the ANN model through the c/python API of the TensorFlow framework. Then, apply the ANN-improved $k$-$\omega$ SST turbulence model to other unseen cases.

## III. NUMERICAL RESULTS AND DISCUSSION

In this section, we validate the ANN-improved $k$-$\omega$ SST turbulence model by simulating two typical sets of separated flow problems: the separated flow over slopes and steps at low Reynolds numbers and the separated flow over airfoils at high Reynolds numbers. Our research pays special attention to evaluating the model's generalization and convergence capabilities, ensuring a comprehensive assessment of its performance.

### A. Separated flows over slopes and steps

The framework is first applied to simulating separated flows over slopes and steps, which are commonly used for validating data-driven turbulence modeling due to its rich high-fidelity turbulence database at a wide range of Reynolds numbers [10,12,49]. We selected flow past the periodic hills (PHs) at $\mathrm{Re}_h = 5600$ for model training and flows over PHs, backward-facing step (BFS) without curve at $\mathrm{Re}_h = 5000$, and slopes (a bump at $\mathrm{Re}_h = 25\,000$ and a curved backward-facing step (CBFS) at $\mathrm{Re}_h = 13\,700$) for validation.

#### *1. Case setting and model training on multiple shapes and cases*

The PH cases are a widely used benchmark in computational fluid dynamics for studying turbulent separated flows. It involves a series of sinusoidal hills that create flow separation and reattachment, characterized by adverse pressure gradients and recirculation zones. This challenging test case provides insights into the accuracy of turbulence models, particularly in predicting separation and reattachment. Xiao *et al.* [49] parametrized the geometry of the PH based on steepness ratios $\alpha$ and provided extensive DNS flow field data. The parameter $\alpha$ alters the hill's steepness and the geometry's overall length while the height remains unchanged. It has a noticeable effect on the behavior of separating flows. In this work, we selected shape parameters corresponding to

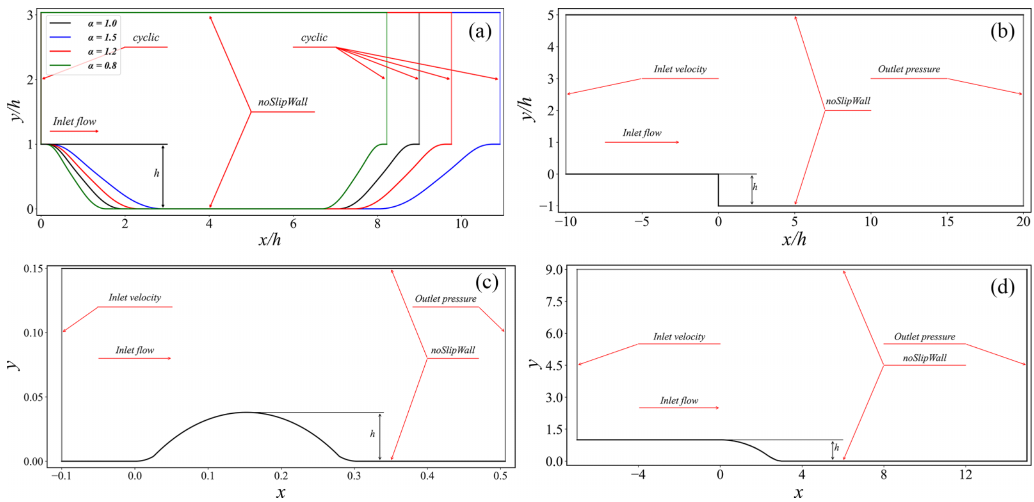

FIG. 3. Schematic of the geometries of (a) PHs, (b) a BFS, (c) a bump, and (d) a CBFS.

$\alpha = 0.8$, 1.0, 1.2, and 1.5. Among them, the cases of $\alpha = 1.0$ and 1.5 are selected for training the model, while the others are chosen as test cases, as shown in Fig. 3(a). The left and right sides are connected to achieve periodicity. Hence, the cyclic boundary conditions are used at the inlet (left side) and outlet (right side). The BFS case, which differs most significantly from the training data in its geometry due to the absence of curvature, is chosen to assess the generalizability of the improved model, as illustrated in Fig. 3(b). The geometry, DNS results, and experimental data are sourced from Refs. [50,51]. In addition, the parametric bumps [52] with maximum heights of 38 mm and the CBFS case [53], which exhibit notable differences in shape, incoming flow, and boundary conditions compared to the PHs, are chosen to further assess the generalization capability of the ANN-improved SST turbulence model, as illustrated in Figs. 3(c) and 3(d). Additionally, Table II provides detailed parameters for the training and testing cases, and the computational grids are presented in the Appendix.

For the training process, the ensemble's sample number is 24. The dafi code can easily assign a separate thread to each sample for parallel computation. The Gaussian distribution with a slight variance is selected as the initial sample to avoid inversion instability caused by a large Kalman gain matrix. The relative standard deviation of the initial parameter is set as 0.1. The simple network structure for the ANN will make it challenging to map the nonlinear relationship between the local dimensionless field quantity and the corrected field. On the contrary, the overly complex network structure will also cause overfitting. Therefore, the ANN model containing four hidden layers with eight nodes per layer is employed for this case, and the leaky Rectified Linear Unit (RELU) activation function is used at each artificial neuron. The regularization parameter $\lambda$ used in this work is employed to adjust the weight of the regularization term in the cost function. It is set as 0.03 in

TABLE II. Summary of rear slope separation flow cases used for training and testing.

| Case | Use | Geometry | Re | Inlet velocity (m/s) |
|---|---|---|---|---|
| PHs | Training | $\alpha = 1.0, 1.5; h = 1$ m | 5 600 | 0.028 |
| PHs | Testing | $\alpha = 0.8, 1.2; h = 1$ m | 5 600 | 0.028 |
| BFS | Testing | $h = 1$ m | 5 000 | 1.000 |
| CBFS | Testing | $h = 1$ m | 13 700 | 1.042 |
| Bump | Testing | $h = 38$ mm | 25 000 | 16.68 |

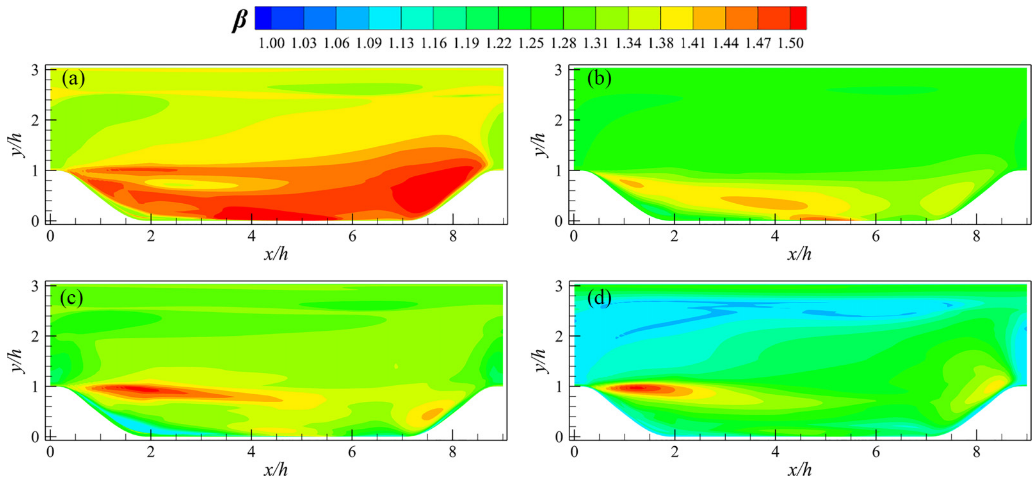


FIG. 4. The correction field $\beta$ of the PH with different $\lambda$ for PHs: (a) $\lambda = 0$, (b) $\lambda = 0.015$, (c) $\lambda = 0.030$, and (d) $\lambda = 0.045$.

this case. We discuss the effect of different $\lambda$ on the distribution of the correction fields $\beta$. Figures 4 and 5 present the contour and probability density of $\beta$ for different regularization parameters. The mathematical expectations for the approximate Gaussian distribution corresponding to the different regularization parameters $\lambda$ are $\mu_a = 1.406$, $\mu_b = 1.304$, $\mu_c = 1.281$, and $\mu_d = 1.205$, respectively. As the weight of the regularization term increases, the range and magnitude of corrections to the disturbance term are significantly reduced. Moreover, as $\lambda$ increases, the proportion of

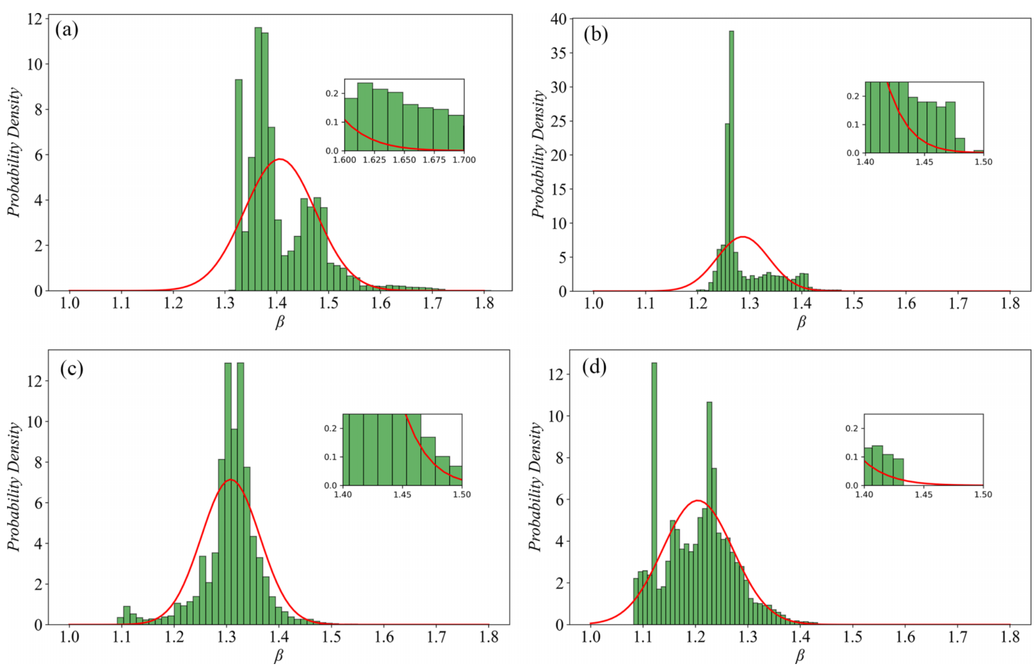


FIG. 5. The probability density of $\beta$ at different $\lambda$ (the red line represents an approximate Gaussian distribution): (a) $\lambda = 0$, (b) $\lambda = 0.015$, (c) $\lambda = 0.030$, and (d) $\lambda = 0.045$.

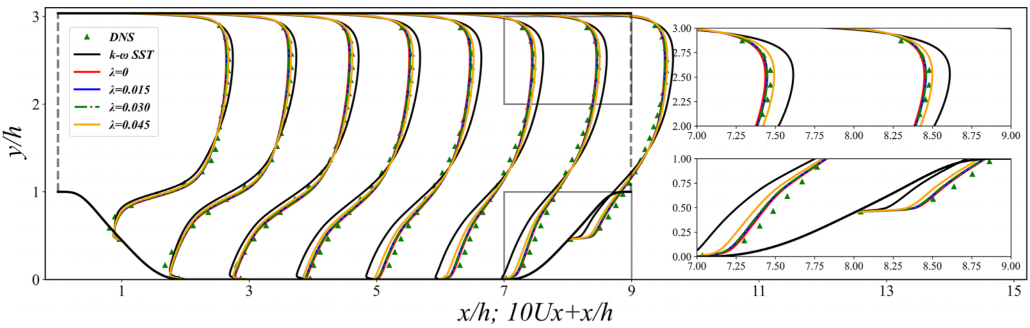


FIG. 6. The comparison of the velocity profiles for different regularization parameters.

the regularization term in the process of inversion optimization will increase, and the error between the solver's output and the values of the observational term also changes accordingly. Figure 6 intuitively shows the impact of different regularization parameters on the prediction accuracy of different profiles. As $\lambda$ increases, the constraint imposed by the regularization term may lead to an increase in observation space error. When $\lambda = 0.045$, although there is still a noticeable improvement over the baseline model, the error increases significantly compared to the other three modified models. We believe that for $\lambda \leqslant 0.045$, the introduction of the regularization term does not negatively impact the optimization in the observational space. Therefore, we determined that $\lambda = 0.03$ provides the optimal correction.

In this work, thanks to the derivative-free and Bayesian nature of the Kalman method, unlike the traditional direct data-driven neural network turbulence closure model, sparse and even noisy indirect data can be used for model training, the nondimensional mean velocities at $x/h = 1, 3, 5, 7$ are extracted as the observation data, and the mean DNS data are interpolated to observation points. The observational term in the cost function represents the velocity error between the DNS and the result of the solver embedded with the ANN model. Accordingly, it is defined as

$$\mathscr{J}(\boldsymbol{\chi})=||\boldsymbol{\chi} - \boldsymbol{\chi}^f||^2_{\mathbf{P}^{-1}} + ||u^{\mathrm{DNS}}/u_{\mathrm{inlet}} - \boldsymbol{\xi}(\boldsymbol{\chi})||^2_{\mathbf{\Gamma}^{-1}} + ||\beta - 1||^2_{\mathbf{Q}^{-1}}, \tag{22}$$

where $u^{\mathrm{DNS}}$ represents the DNS velocity in observational space, $u_{\mathrm{inlet}}$ represents the inlet velocity. Figure 7 shows the iteration convergence history of the REKI loop. After ten steps, the REKI calibration process converges, with the cost function decreasing from 10.11 to 1.29 (a reduction of 86.15%), and the error in the observation space decreasing from 0.31 to 0.028 (a reduction of

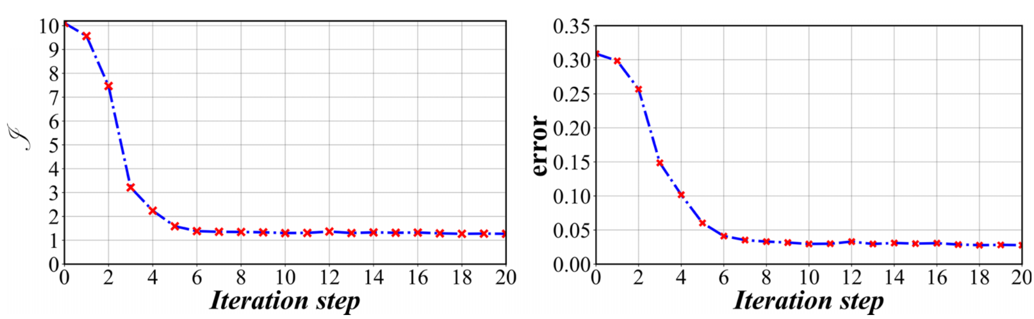


(a) Step versus cost function

(b) Step versus **error**

FIG. 7. The convergence history of the REKI calibration process for periodic hills.

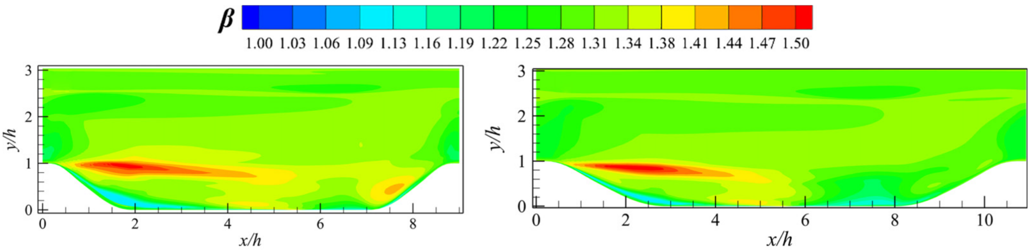


(a) α=1.0 (b) α=1.5

FIG. 8. Correction field $\beta$ of the periodic hills with different steepness ratios.

90.9%). The error in the observation space is defined as

$$\textbf{error} = \frac{1}{N}\sum_{n=1}^{N}\left|\left(u_n^{\mathrm{DNS}} - u_n^{\mathrm{REKI}}\right)/u_{\mathrm{inlet}}\right|, \tag{23}$$

where $N$ represents the number of observation points.

After the convergence of the ensemble, we couple the trained model with the RANS solver and apply the model to simulate the training cases first. Figure 8 shows the correction field $\beta$ of two training cases, where the corrections are most active in the shear layer of the separation region, the correction above the separation area is significantly greater than 1.0 at $x/h = 0$–4, and its maximum value is approximately 1.5. $\beta > 1.0$ indicates a more pronounced disturbance in the transport equation, altering the overall balance of turbulence flow. This correction results in a lower dissipation rate and higher turbulent kinetic energy. As illustrated in Fig. 9, the improved turbulence model predicts significantly higher turbulent kinetic energy compared to the baseline turbulence model and is closer to DNS results, where the turbulent kinetic energy is normalized by inlet velocity. It is worth emphasizing that turbulent kinetic energy is not used as a constraint in the cost function. Additionally, the improved velocity fields and streamlines in the separation

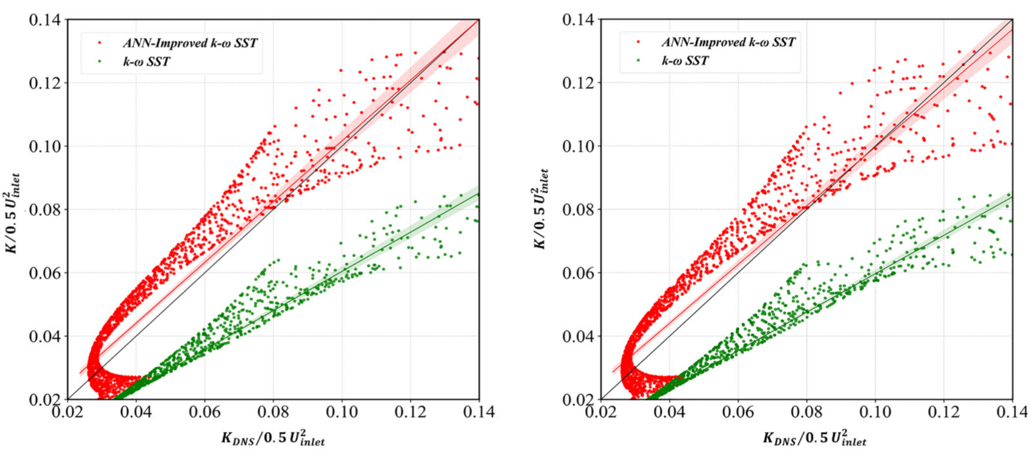


(a) α=1.0 (b) α=1.5

FIG. 9. The comparison of turbulent kinetic energy between RANS with different turbulence models and DNS for periodic hill cases on every grid for training cases, where the DNS turbulent kinetic energy is interpolated onto the RANS grid (red points, DNS versus improved SST; green points, DNS versus baseline SST).

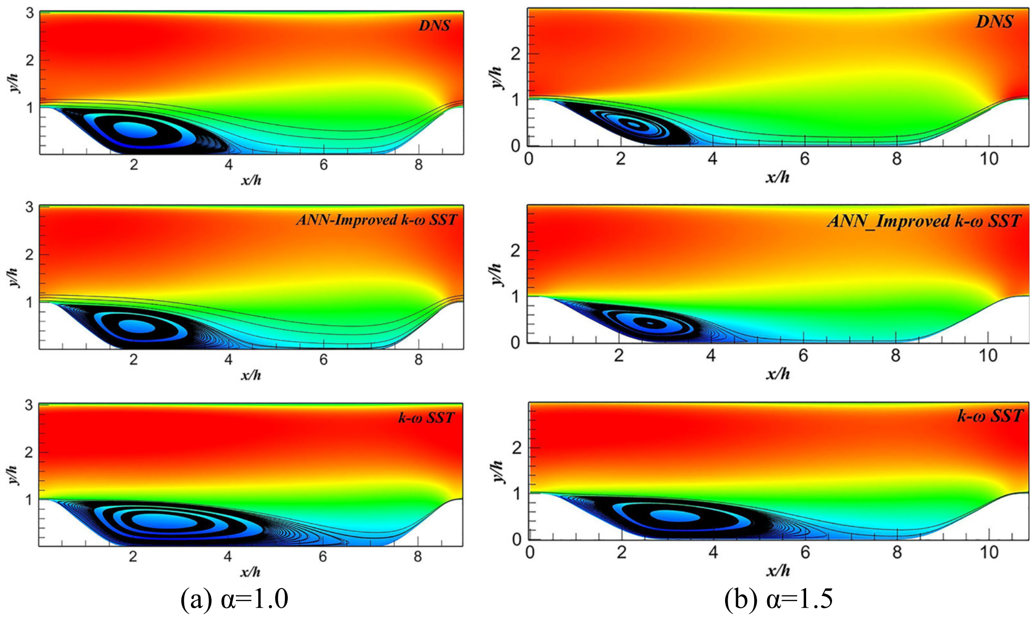

FIG. 10. The comparisons of velocity distributions and streamlines of different models in training sets.

area, compared with the DNS data and the results obtained by the baseline turbulence model, are presented in Fig. 10. The streamline resulting from DNS data shows that the baseline RANS model overestimates the size of the separation bubble, revealing that the baseline turbulence model is not capable of precisely capturing the flow separation feature for this case. In contrast, the improved turbulence model provides higher turbulent kinetic energy, increasing shear stress and promoting the separated flow's reattachment. The separation point and size of the separation bubble agree well with the DNS results.

To provide a more intuitive and quantitative comparison of the prediction accuracy between the two models, Fig. 11 represents the velocities in the $x$ direction along various profiles ($\alpha = 1.0$, $x/h = \{1, 2, 3, 4, 5, 7, 8, 9\}$; $\alpha = 1.5$, $x/h = \{1, 2, 3, 4, 5, 6, 7, 8, 9\}$). The results obtained by the baseline turbulence model deviate significantly from the DNS result. In contrast, the improved turbulence model shows a remarkable improvement in the velocity profiles throughout the flow region. Figure 12 shows the comparisons of the skin friction coefficient. The results show that only

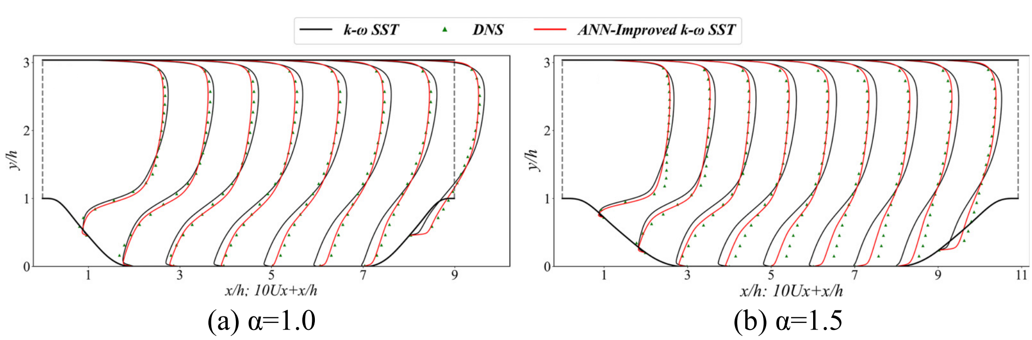

FIG. 11. The comparisons of normalized velocity profiles of different models for PH cases in training sets.

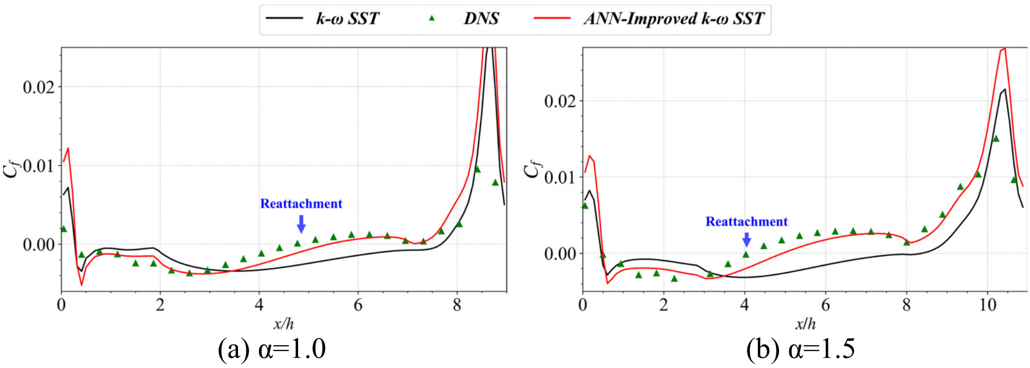


FIG. 12. The comparisons of skin friction coefficient of different models for PH cases in training sets.

the velocity as the observation data to guide the ANN model promotes the reattachment of the flow and significantly improves the prediction accuracy of the friction coefficient to some extent.

### *2. Generalization and convergence verification*

As discussed in Sec. III A 1, the ANN-improved $k$-$\omega$ SST turbulence model with the proposed training framework shows promising improvements in predictive accuracy. Furthermore, to assess whether the improved turbulence model can improve accuracy for an unseen case, an evaluation is conducted to determine if the model's performance can be generalized to other scenarios. The first two test cases are PHs of $\alpha = 0.8$ and 1.2, with different channel lengths and hill slopes compared to the training cases. Although similar to the training cases, the separated flow is susceptible to the shape parameter $\alpha$, especially the slope change. Figure 13 shows the comparison of normalized velocity under different profiles ($\alpha = 0.8, x/h = \{1, 2, 3, 4, 5, 6, 7\}$; $\alpha = 1.2, x/h = \{1, 2, 3, 4, 5, 6, 7, 8\}$) in the test cases. Note that the case with $\alpha = 0.8$i is actually not covered by the parameter spanned over the training set. Even with this deviation, good agreements between the present results and the DNS data have been achieved, indicating the reliability of the proposed ANN-based method for simulating turbulence flows with separations with different geometries. The result demonstrates the generalization ability of the ANN-mproved $k$-$\omega$ SST turbulence model to different shapes.

To further assess the improved turbulence model's ability to generalize, we apply it to the BFS, CBFS, and bump cases with significant differences in shape, inflow, and boundary conditions. Unlike the PH cases' cyclic inflow and outflow, these involve a fully developed velocity inlet and

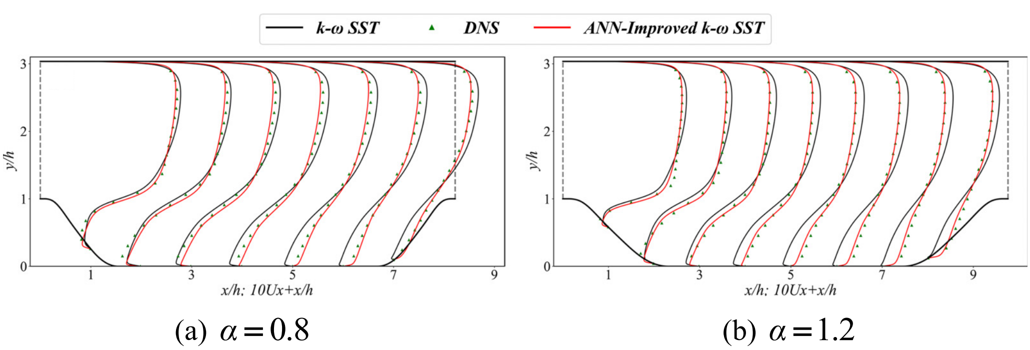


FIG. 13. The comparisons of normalized velocity profiles of different models for PH cases outside the training set.

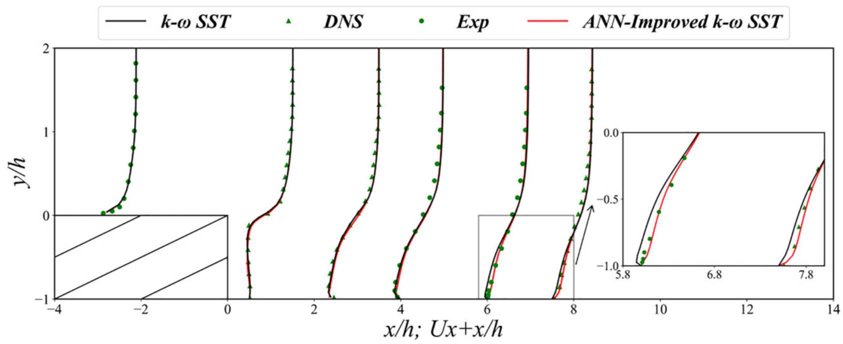


FIG. 14. The comparisons of normalized velocity profiles with different models.

pressure outlet. For the BFS case, Fig. 14 presents the velocity comparison at different stations. The improved model significantly enhances the prediction accuracy in the reattachment region. Additionally, it is worth noting that the modified model does not disrupt the boundary layer region on the upstream side of the step, as evidenced by the comparison of the velocity distribution at $x/h = -3.0$. Figure 15 shows the streamline distribution of the separation zone. The results visually demonstrate that the improved model significantly improves the prediction accuracy in the attached area, with the data closer to the experimental values at $x/h = 6.0$. Figure 16 shows the correction field; similar to the PHs, the correction above the separation area ($x \in (2, 4)$) is significantly larger than 1.0. Figure 17 shows streamlines in the separation zone of different turbulence models. Figure 18 presents the normalized velocity profiles in the separation zone (bump, $x = \{0.2, 0.3, 0.4, 0.5\}$, $y \in (0, 0.05)$; CBFS, $x/h = \{-1.0, 1.0, 2.5, 3.5, 5.0, 6.0\}$, $y/h \in (0, 2.0)$) with different models, and Fig. 19 presents the comparisons of the skin friction coefficient of different models. These results indicate that the improved turbulence model still significantly improves separation prediction capability despite the vast differences between the test and training scenarios, further proving the improved turbulence model's generalization ability.

In this work, we multiply the ANN model by a relaxation function that varies with the iteration steps to improve the convergence speed, which can be expressed as $\beta(\boldsymbol{\eta}) = 1 + \tanh(i/b)\boldsymbol{f}$, where $i$ is the solver's iteration step and $b$ is set as 1000 for all cases. As the number of iterations increases, $\tanh(i/b)$ approaches 1.0, becoming equivalent to the trained ANN model. This prevents unreasonable model corrections from earlier flow field discrepancies, accelerating convergence. Figure 20 compares the convergence processes of different models for the PH case with $\alpha = 1.5$, showing that introducing the relaxation function improves convergence speed. We compared the convergence history curves at different mesh resolutions and Reynolds numbers, as shown in Fig. 21. As the Re decreases, the convergence of the improved model gradually approaches that of the baseline model. A lower mesh resolution accelerates the convergence speed but results in higher stabilized residuals.

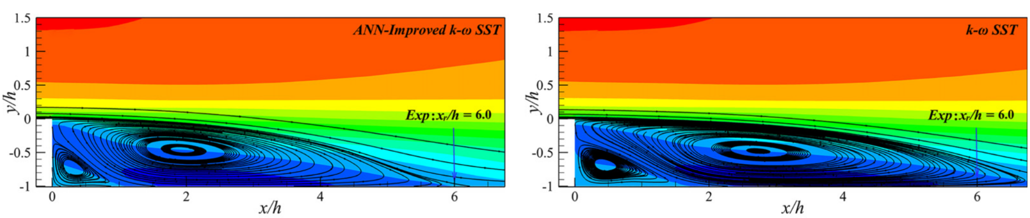


(a) ANN-Improved $k$-$\omega$ SST (b) $k$-$\omega$ SST

FIG. 15. The comparisons of velocity distributions and streamlines of different models on a BFS.

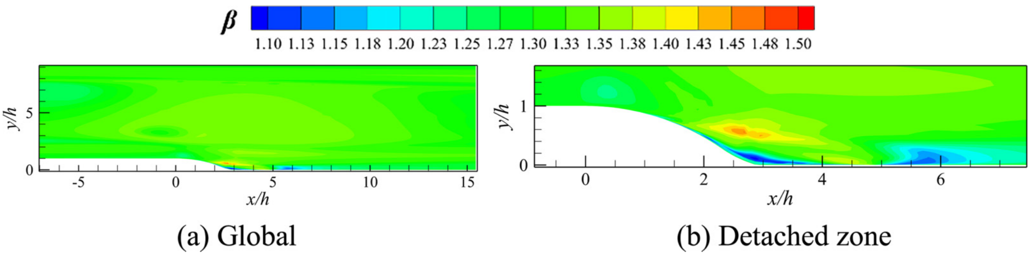


FIG. 16. Correction field $\beta$ of the CBFS case.

Figure 22 presents the convergence rate for the baseline turbulence model and the improved turbulence model for PH and bump cases. For the bump case, the improved turbulence model displays comparable convergence characteristics to the baseline turbulence model. For the PH case with $\alpha = 1.0$, the two models exhibit almost identical convergence rates. In summary, the ANN-improved turbulence model shows good convergence for rear slope separation flow with a low Reynolds number, and its convergence efficiency falls well within the acceptable range. Additionally, it is worth emphasizing that although the ANN-improved turbulence model may take extra time to call the ANN model in the iteration process, compared with the baseline turbulence model, the calculation time required to converge to a residual value benchmark is basically in the order of magnitude for different mesh resolutions as shown in Fig. 23 (a residual convergence of $10^{-7}$ is considered to indicate that the average flow field remains almost stable). Therefore, the computational efficiency is significantly improved relative to the DNS or LES.

### B. Flow over airfoils with high Reynolds numbers

In Sec. III A, multiple examples demonstrate a significant improvement in the accuracy of the ANN-improved $k$-$\omega$ SST turbulence model for low Reynolds number cases. However, the

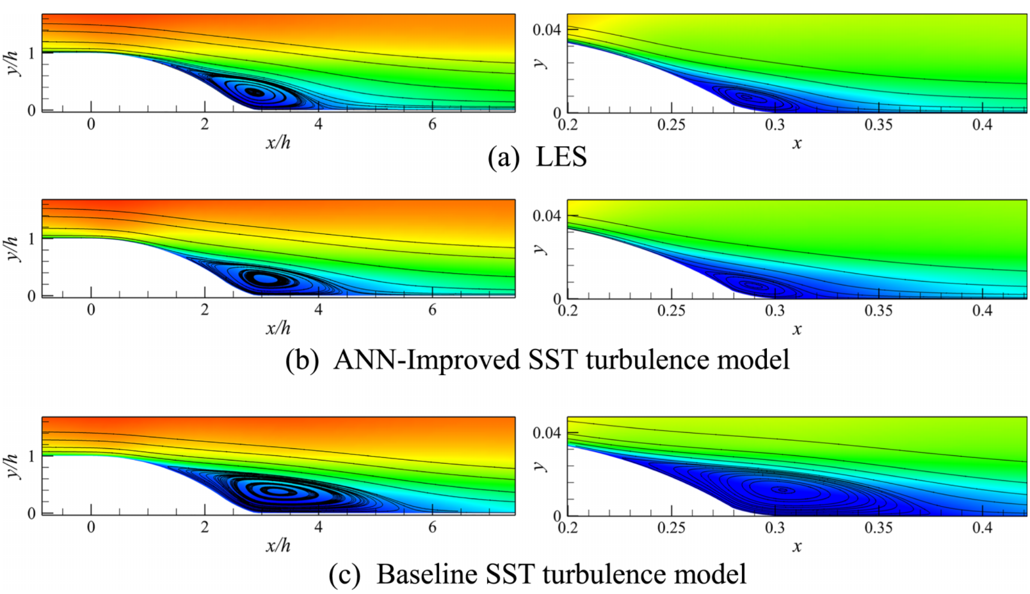


FIG. 17. The comparisons of velocity distributions and streamlines of different models on different test cases (left, CBFS; right, bump).

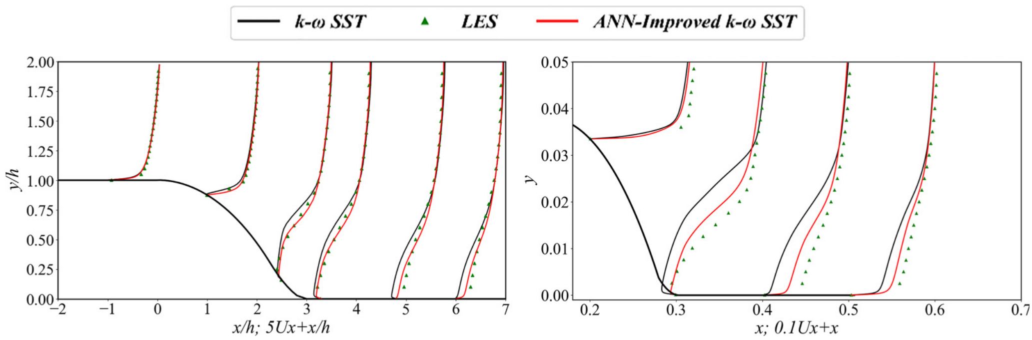

(a) CBFS (b) Bump

FIG. 18. The comparisons of normalized velocity profiles from different models with different cases.

limitations of LES and DNS for high Reynolds number cases resulted in a lack of turbulence databases, making it challenging for traditional turbulent closed terms' data-driven direct modeling. On the other hand, even with the FIML framework, using experimental data for inversion training still does not directly consider the coupling effects between the model and the RANS solver, which may result in error amplification due to numerical iteration, especially at high Reynolds iteration. The present improved framework based on integrating field inversion and machine learning addresses the drawbacks of the above modeling methods. Therefore, evaluating the performance of the proposed framework under high Reynolds number flow becomes crucial. The wind turbine airfoils, including S809, S805, and S814 airfoils with Reynolds numbers ranging from $1.0 \times 10^6$ to $3.0 \times 10^6$, are utilized for validation. This choice is motivated by the availability of extensive experimental data, which is crucial for supporting the inverse training process [54–56], where the Reynolds number is based on the inlet Mach number and the chord length of the airfoil.

### *1. Case setting and model training on multiple angles of attack*

In the case of these wind turbine airfoils, as the angle of attack increases, the separation flow becomes more pronounced, making it difficult for traditional RANS models to predict accurately. As a result, these airfoils are widely used for turbulence modeling of high Reynolds number separated flows [15,17,32]. Figure 24 presents the geometry of the wind turbine airfoils for validation.

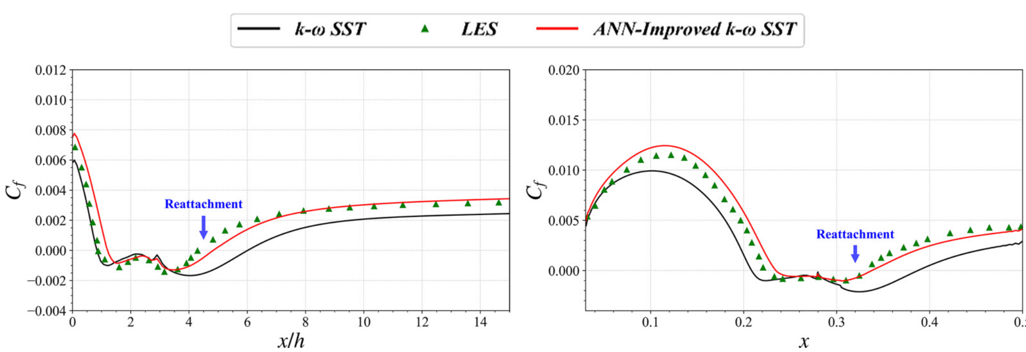

(a) CBFS (b) Bump

FIG. 19. The comparisons of skin friction coefficient from different models with different cases.

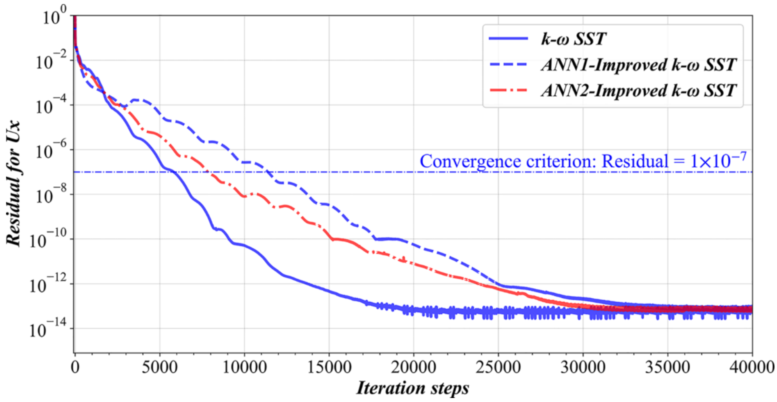


FIG. 20. The comparison of convergence processes between different models for a periodic hill with $\alpha = 1.5$ (ANN1, $b = 1$; ANN2, $b = 1000$).

For this inversion problem, the upper wall pressure coefficient is chosen as the observation data, ensuring that the trained ANN-improved *k*-*ω* SST model can accurately capture the reverse pressure gradient. The pressure coefficient corresponding to the wall grid node is interpolated to the position of the experimental measurement point. For airfoils, the correction near the wall is crucial, and

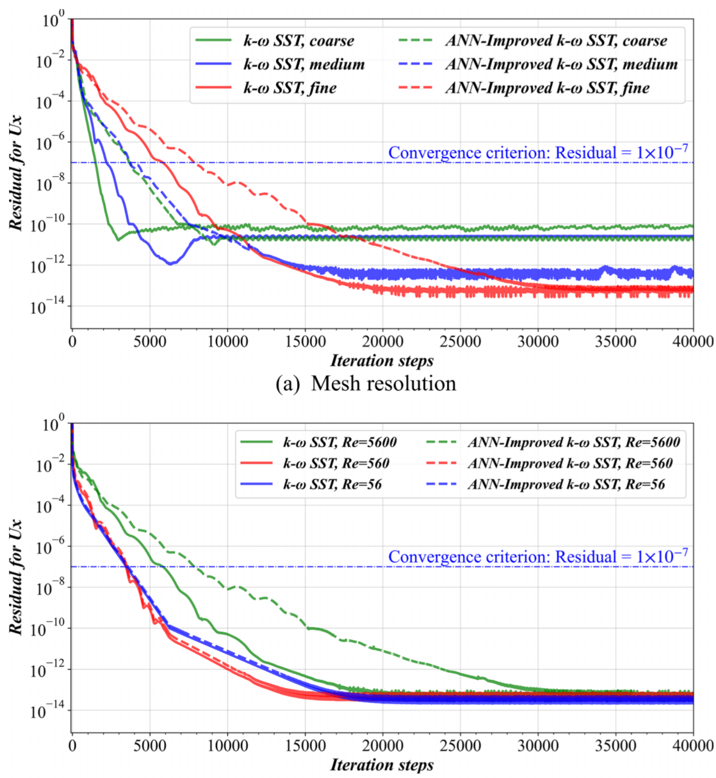


(a) Mesh resolution

(b) Re

FIG. 21. The residual plots in converging history of different mesh resolution and Re for a periodic hill with $\alpha = 1.5$.

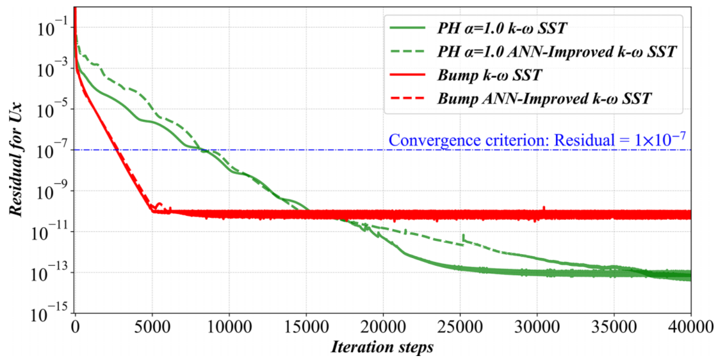


FIG. 22. The residual plots in converging history of different turbulence models on bump and PH cases.

extending the correction region beyond one chord length did not result in significant accuracy improvements, according to our tests. Therefore, only the area within one chord length from the wall is corrected to save computational resources, and the far field is set to the default value of 1. Additionally, the S809 airfoil at multiple angles of 8.2° and 14.2° are selected as training cases, as shown in Table III, where the former has almost no flow separation, while the latter exhibits apparent flow separation. This selection method ensures good computational accuracy of the model, regardless of the presence or absence of flow separation.

The number of samples in the ensemble is 24, and the relative standard deviation of the initial parameter is set as 0.008. In addition, the regular constant $\lambda$ in the regular term is set as 0.003. A longer iteration step means that the $S$ and $d$ in the regularization term are also adjusted appropriately to avoid the constraint term dominating prematurely. The $S$ and $d$ are set as 30 and 2, respectively.

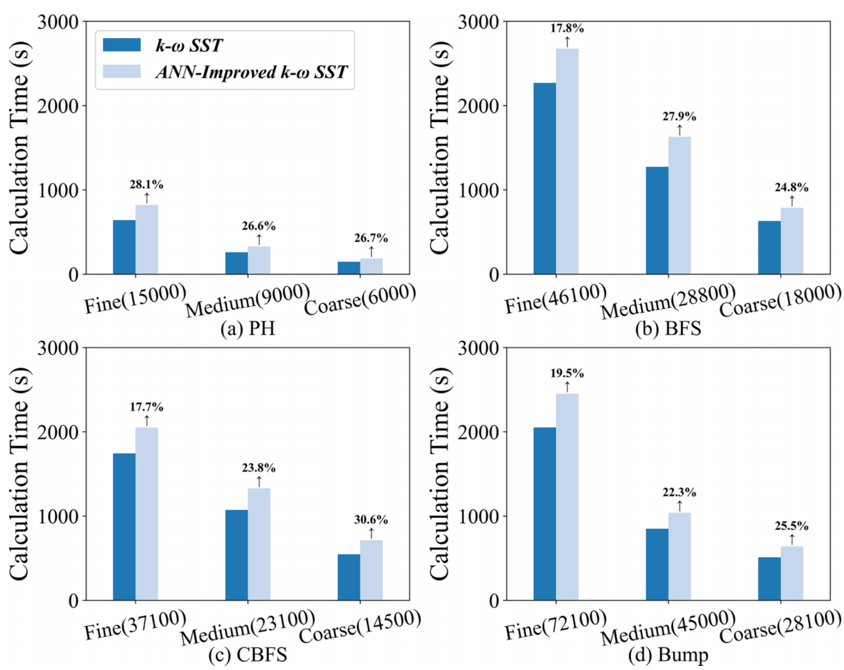


FIG. 23. The relationship between the calculation time required for convergence to $10^{-7}$ and mesh resolution (the mesh counts are shown in parentheses).

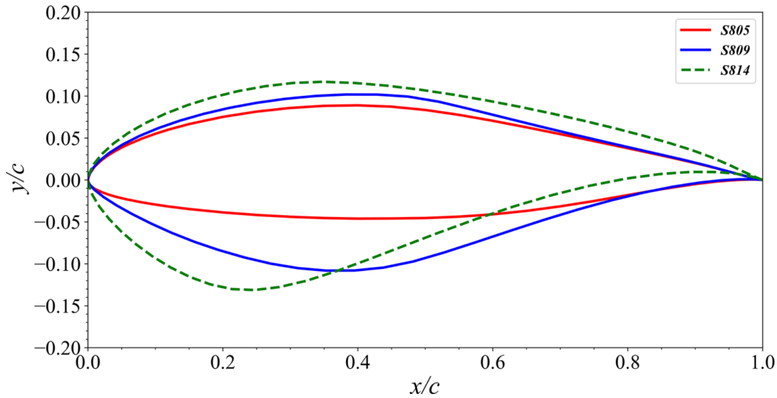


FIG. 24. The geometry of the wind turbine airfoils.

Here, the cost function is defined as

$$\mathscr{J}(\boldsymbol{\chi}) = ||\boldsymbol{\chi} - \boldsymbol{\chi}^f||^2_{\mathbf{P}^{-1}} + ||\boldsymbol{C_P}^{\text{expt}} - \boldsymbol{\xi}(\boldsymbol{\chi})||^2_{\boldsymbol{\Gamma}^{-1}} + ||\beta - 1||^2_{\mathbf{Q}^{-1}}, \tag{24}$$

where $\boldsymbol{C_P}^{\text{expt}}$ represents the experimental pressure coefficient. The observational term represents the upper wall pressure coefficient error between the experience and the solver's output. Figure 25 shows the iteration convergence history of the REKI loop for the S809 airfoil. After 100 steps, the REKI calibration process converges, with the cost function decreasing from 0.95 to 0.098 (a reduction of 89.6%), and the error in the observation space decreasing from 0.11 to 0.0048 (a reduction of 95.6%). The error in the observation space is defined as

$$\textbf{error} = \frac{1}{N}\sum_{n=1}^{N}\left|\boldsymbol{C_{P_n}}^{\text{expt}} - \boldsymbol{C_{P_n}}^{\text{REKI}}\right|, \tag{25}$$

where $N$ represents the number of observation points.

After training, the coupled ANN-improved turbulence model can be easily employed in other cases. Figure 26 shows the streamlines of the separation vortex of the S809 airfoil at the angle of attack of 14.2° calculated by the improved turbulence model and the baseline turbulence model. The separation vortex calculated by the improved turbulence model is larger than the baseline turbulence model. Figure 27 intuitively shows the comparisons of the wall pressure coefficient of different turbulence models. For cases at the angle of attack of 8.2° where separation does not occur, the pressure coefficients computed by both models are consistent with the experimental data. As the angle of attack increases, there is a significant separation flow at the airfoil's trailing edge, and the baseline turbulence model cannot accurately calculate the size of the separation vortex. The improved turbulence model can still accurately capture the separation vortex by comparing it with experiments.

TABLE III. Summary of high Reynolds number cases used for training and testing.

| Case | Use | Angle of attack (deg) | $\mathrm{Re}/10^6$ | Inlet Mach number |
|---|---|---|---|---|
| S809 | Training | 8.2,14.2 | 2.0 | 0.15 |
| S809 | Testing | 0–18.2 | 1.0, 1.5 | 0.15 |
| S805 | Testing | 0–18.2 | 1.0, 2.0 | 0.15 |
| S814 | Testing | 0–18.2 | 1.0, 2.0, 3.0 | 0.15 |

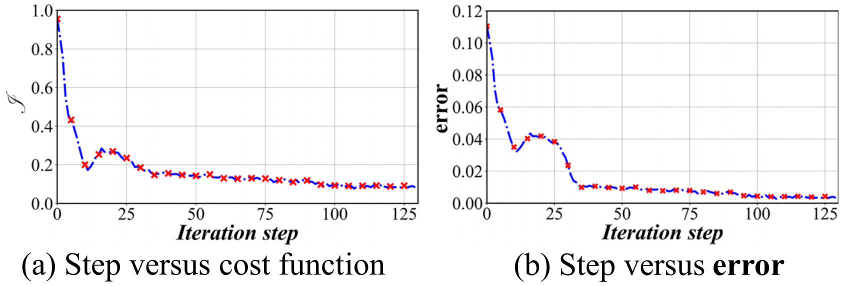


FIG. 25. The convergence history of the REKI calibration process for the S809 airfoil.

### 2. *Generalization performance and convergence verification*

In this section, to verify the generalization ability of the ANN-improved turbulence model under the separation flow with a high Reynolds number, the improved turbulence model is further applied to the S809 airfoil at angles of attack outside the training set. Figure 28 presents the correction field $\beta$ of the S809 airfoil at angles of attack of 12.2° and 18.2°. Contrary to the cases in Sec. III A, the baseline turbulence model predicts a relatively small separation vortex for the high Reynolds number airfoil separation problem at large angles of attack. Consequently, the improved turbulence model calculates the correction field $\beta$ that is less than 1.0 in the separation region, particularly near the trailing edge. Its minimum value is approximately 0.75. As the angle of attack increases, the correction range also expands significantly. This behavior is beneficial for preventing flow reattachment in the separation vortex region. Figure 29 shows the profiles of velocity and eddy viscosity near the upper wall of the S809 airfoil. The improved model enhances the prediction of eddy viscosity in the trailing edge separation region of the airfoil while remaining consistent with the baseline model in other regions, promoting premature separation, as presented in Fig. 29(b). Figures 30 and 31 present different turbulence models' streamlines and pressure coefficients. For the S809 airfoil at angles of attack outside the training sets ($\alpha = \{0°, 12.2°, 16.2°, 18.2°\}$), the improved turbulence model can achieve accuracy comparable to experimental data, regardless of whether the separated flow is present. The results demonstrate that the improved model exhibits strong generalization capabilities, even with variations in the angle of attack.

Furthermore, the improved turbulence model is applied to the other airfoil at multiple angles of attack, which differed from the S809 airfoil with different Reynolds numbers, incoming Mach numbers, and geometric shapes. Figures 32 and 33 show the streamlines and the pressure coefficients of varying turbulence models. The improved turbulence model can still compute satisfactory results, albeit with significant deviations from the training set. The results further powerfully demonstrate the generalization ability of the improved turbulence model.

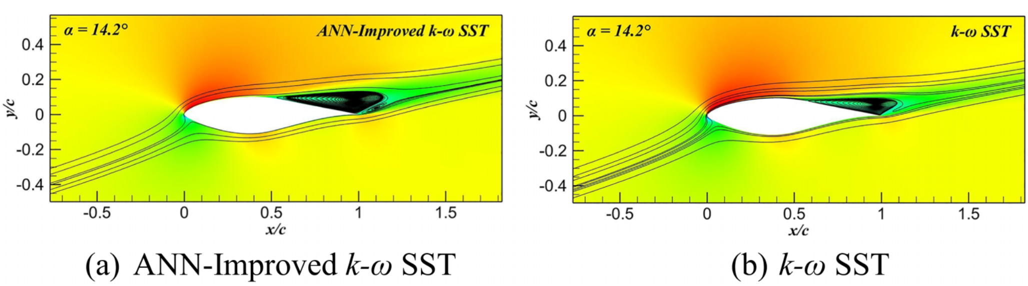


FIG. 26. The comparisons of velocity distributions and streamlines of different models for the S809 airfoil at Re $= 2.0 \times 10^6$.

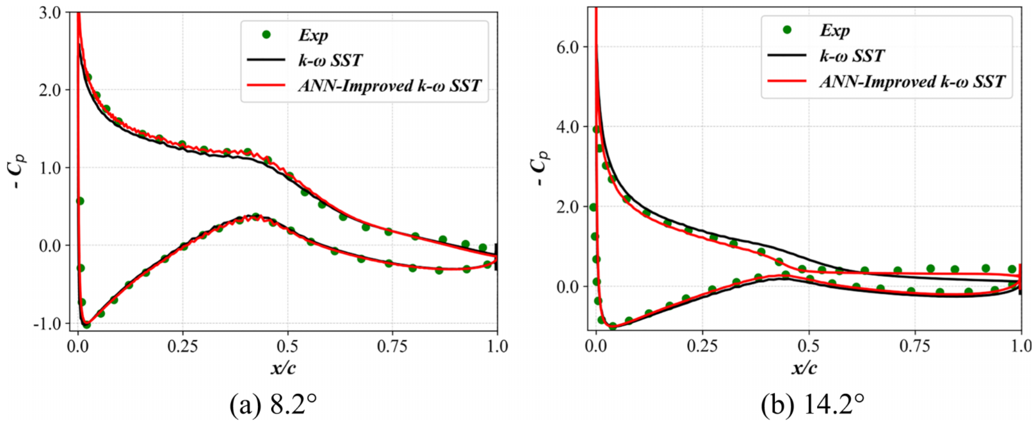


FIG. 27. The comparisons of the wall pressure coefficient of different models for the S809 airfoil at Re $= 2.0 \times 10^6$.

Figure 34 compares the lift coefficients at different angles of attack between experimental data and numerical results. The improved model significantly improves the prediction of stall. From the results, under the condition of apparent separation, the improved turbulence model significantly enhances the accuracy of numerical simulation. In contrast, the improved turbulence model can still maintain accuracy comparable to the baseline turbulence model under no separation.

Figure 35 illustrates the convergence rates for the baseline and improved turbulence models applied to the S809 and S805 airfoils at angle of attack of 14.2°. The improved turbulence model demonstrates convergence rates and residual values comparable to the baseline model for high Reynolds number separated flows. Specifically, the residual of the improved turbulence model drops to less than $1 \times 10^{-7}$ after 40 000 iterations. For the S805 airfoil, the improved model exhibited a faster convergence rate. This convergence rate indicates that the improved turbulence model maintains strong robustness for high Reynolds number separated flow.

## IV. CONCLUSIONS

In this paper, a feature-consistent correction framework with the REKI and ML methodology is presented, aiming to address the issue of insufficient prediction accuracy of the RANS models in simulating separated flows. This approach allows for the simultaneous utilization of DNS results and sparse high-fidelity experimental data in multiple flow conditions to explore the optimal artificial intelligence correction models. Unlike traditional data-driven neural network models that rely on gradient-based backpropagation optimization, the present regularized REKI approach is intrinsically

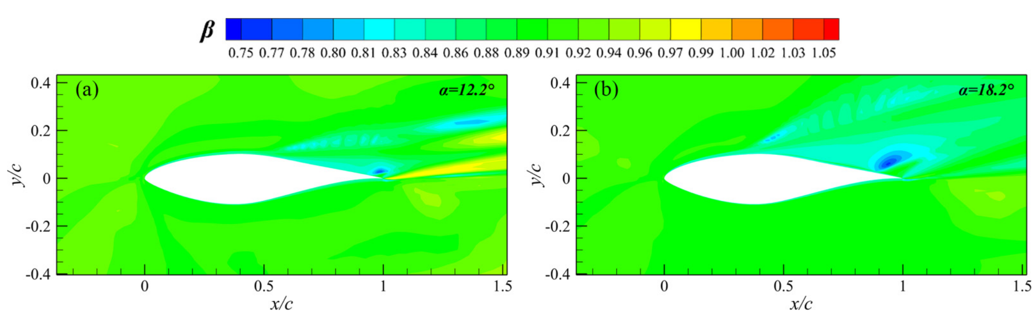


FIG. 28. The correction field $\beta$ of the S809 airfoil at Re $= 2.0 \times 10^6$.

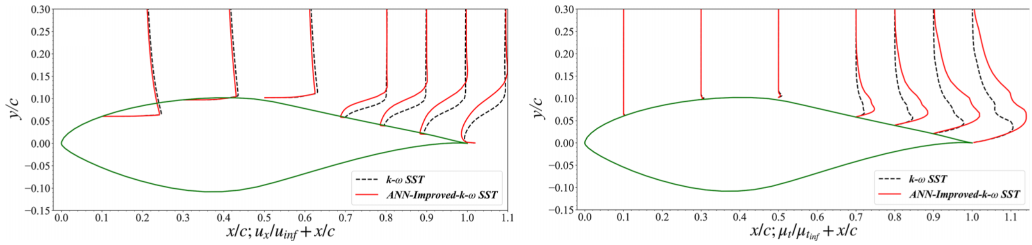


(a) velocity (b) eddy viscosity

FIG. 29. The near-upper-wall eddy viscosity and velocity profiles of different turbulence models for the S809 airfoil at $\alpha = 12.2^\circ$ and $\mathrm{Re} = 2.0 \times 10^6$.

stochastic and gradient-free so that gradient vanishing can be rectified in the training process. The present method also integrates local flow features predicted by the RANS solver at each step of the optimization process and the final trained model. This integration not only enhances the model's generalization ability across different geometries, inflows, and boundary conditions but also guarantees the convergence performance of the RANS solver with the improved $k$-$\omega$ SST turbulence model.

Numerical simulations of two typical sets of separated flow problems, including flows over PHs and slopes and steps at low Re and the separated flow over airfoils at high Re, have been carried out using the present ANN-improved $k$-$\omega$ SST turbulence model. The generalization performance of scenarios with different geometries and Reynolds numbers is carefully examined. Both integral forces and local flow quantities, including pressure distribution, velocity profiles, and skin friction, agree well with the experimental or DNS data quantitatively, demonstrating that the modeling error is substantially reduced. Improved prediction in the recirculation zone and recovery zone is also

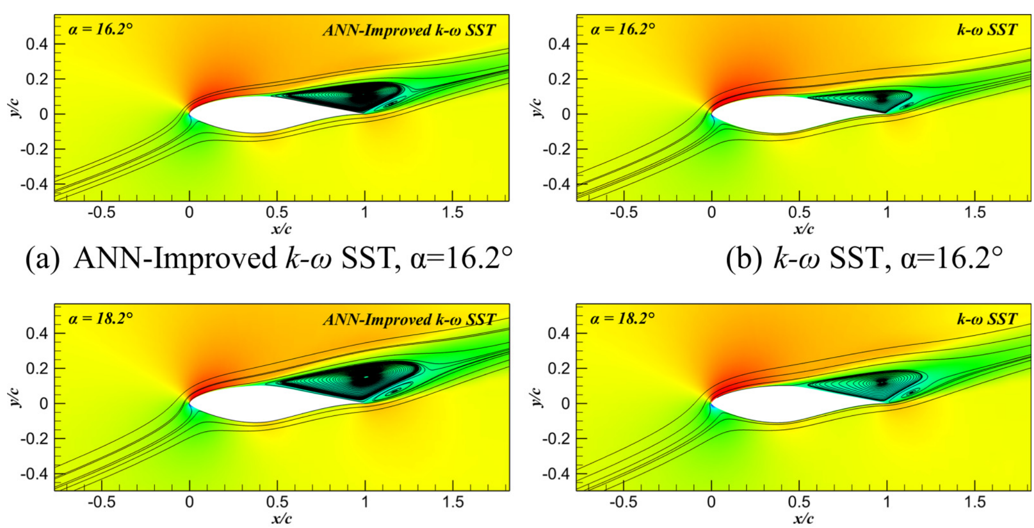


(a) ANN-Improved $k$-$\omega$ SST, α=16.2° (b) $k$-$\omega$ SST, α=16.2°

(c) ANN-Improved $k$-$\omega$ SST, α=18.2° (d) $k$-$\omega$ SST, α=18.2°

FIG. 30. The comparisons of velocity distributions and streamlines of different models for the S809 airfoil at $\mathrm{Re} = 2.0 \times 10^6$.

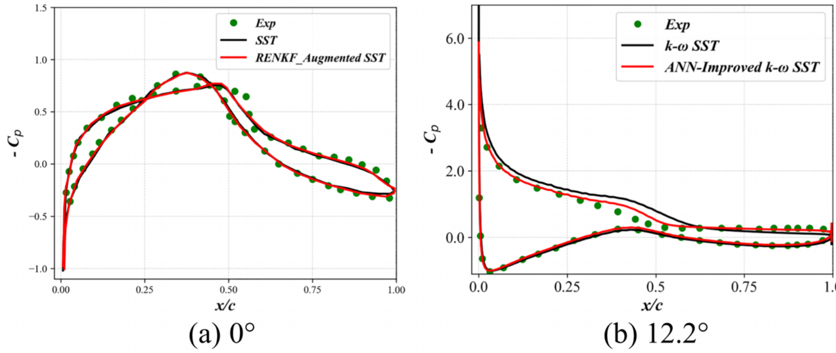


FIG. 31. The comparisons of the pressure coefficients for numerical results with the experimental data for the S809 airfoil at Re $= 2.0 \times 10^6$.

observed. Although the present model is calibrated on the destruction term with multiple flow conditions, the development of a more effective model by considering production, destruction, and diffusion terms in more complex flows can be an important avenue for future studies.

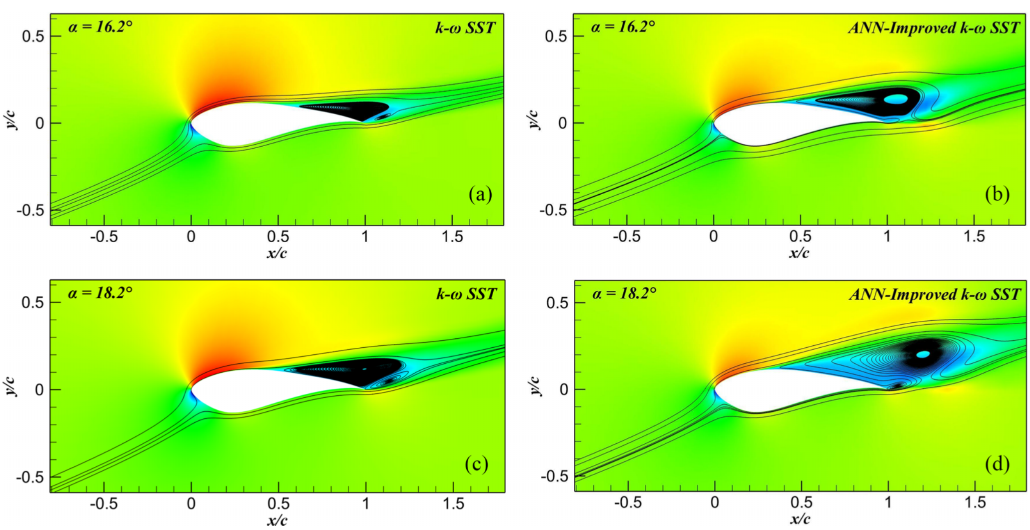


FIG. 32. The comparisons of velocity distributions and streamlines of different models at different angles of attack with the S814 airfoil.

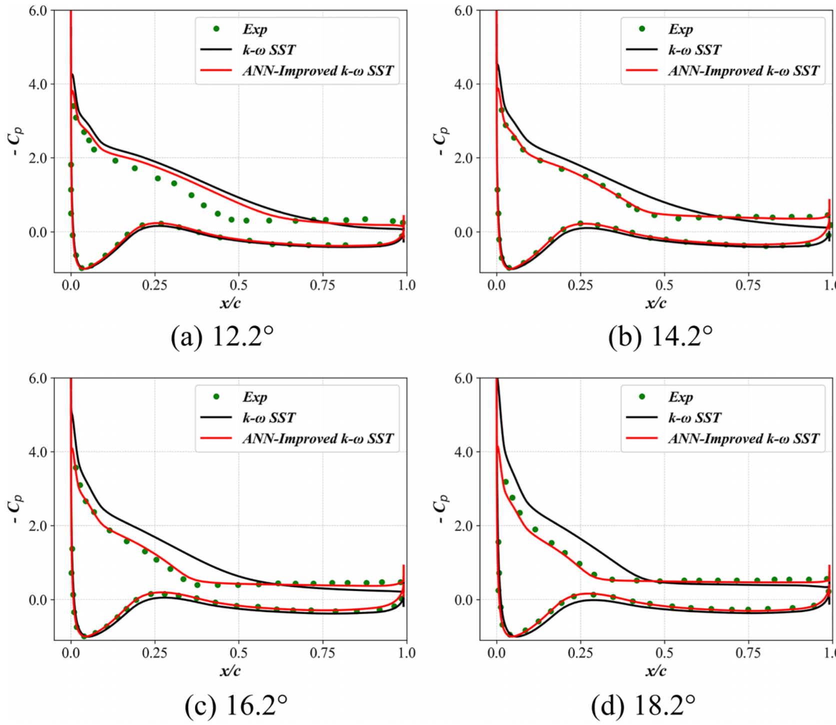


FIG. 33. The comparisons of the pressure coefficients for numerical results with the experimental data for the S814 airfoil at Re $= 2.0 \times 10^6$.

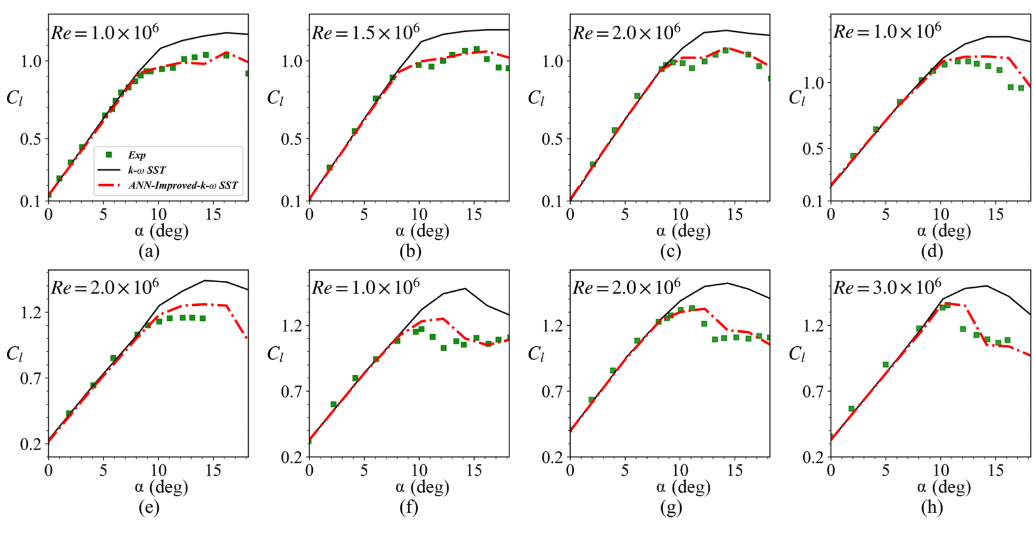


FIG. 34. The comparisons of lift coefficients at different angles of attack between experimental data and numerical results: [(a)–(c)] S809, [(d), (e)] S805, and [(f)–(h)] S814.

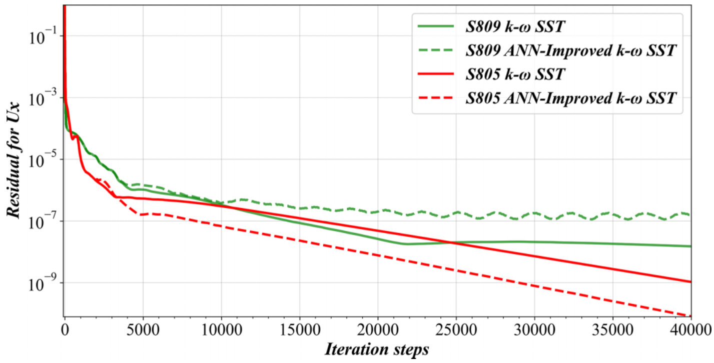


FIG. 35. The residual plots in converging history of different turbulence models at $\alpha = 14.2^{\circ}$: S809, Re $= 2.0 \times 10^{6}$; S805, Re $= 1.0 \times 10^{6}$.

## ACKNOWLEDGMENTS

This work is supported by the National Natural Science Foundation of China (Grant No. 12272178), Aeronautical Science Foundation of China (Grant No. 20220012052004), Key Laboratory of Computational Aerodynamics, AVIC Aerodynamics Research Institute, and the Spring Sunshine Program of the Ministry of Education of China and High Performance Computing Platform of Nanjing University of Aeronautics and Astronautics. We gratefully acknowledge the open-source code dafi and the discussion with the developer, Dr. Xinlei Zhang, and we also want to thank Dr. Hongwei Tang from China Aerodynamic Research and Development Center for the helpful suggestions.

## DATA AVAILABILITY

The data that support the findings of this article are not publicly available upon publication because it is not technically feasible and/or the cost of preparing, depositing, and hosting the data would be prohibitive within the terms of this research project. The data are available from the authors upon reasonable request.

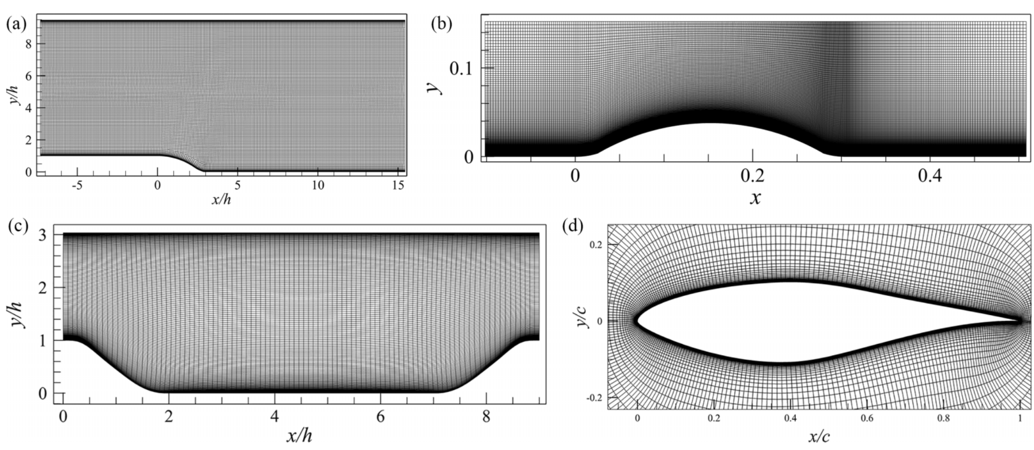


FIG. 36. The computational mesh: (a) CBFS, (b) bump, (c) periodic hill with $\alpha = 1.0$, and (d) S809 airfoil.

## APPENDIX: THE COMPUTATIONAL GRIDS OF CASES

Considering the sensitivity of high-order features to the mesh, this paper adopts the structure mesh to ensure its smoothness. As shown in Fig. 36, in the CBFS case, it adopts a grid of $371 \times 100$, and the maximum $y^+$ of the first layer mesh is 0.91. In the bump case, it adopts a grid of $412 \times 175$, and the maximum $y^+$ of the first layer mesh is 0.93. In the PH cases, it adopts a mesh of $100 \times 150$, and the maximum $y^+$ of the first layer mesh is 0.87. In the S809 airfoil case, it adopts a mesh of $300 \times 150$. There are 50 layers of mesh in the boundary layer with a growth rate of 1.05, and the maximum $y^+$ of the first layer mesh is 0.85. The whole computational domain is a circle whose center is (0 m, 0 m), the radius is 50 m, and the chord length of the airfoil is 1 m. The meshes of all cases satisfy the mesh independence verification.

---


[1] D. J. Mavriplis, Progress in computational fluid dynamics discretizations algorithms and solvers for aerodynamic flows, AIAA J. **59**, 5374 (2021).

[2] F. R. Menter, Two-equation eddy-viscosity turbulence models for engineering applications, AIAA J. **32**, 1598 (1994).

[3] D. C. Wilcox, Reassessment of the scale-determining equation for advanced turbulence models, AIAA J. **26**, 1299 (1988).

[4] P. Spalart and S. Allmaras, A one-equation turbulence model for aerodynamic flows, in *30th Aerospace Sciences Meeting and Exhibit, Reno, NV, USA* (AIAA, Reston, VA, 1992), p. 439.

[5] J. Slotnick, A. Khodadoust, J. Alonso, D. Darmofal, W. Gropp, E. Lurie, and D. Mavriplis, CFD vision 2030 study: A path to revolutionary computational aerosciences, Technical Report NASA CR-2014-218178, NASA (2014).

[6] S. L. Brunton, B. R. Noack, and P. Koumoutsakos, Machine learning for fluid mechanics, Annu. Rev. Fluid Mech. **52**, 477 (2019).

[7] J. Ling, A. Kurzawski, and J. Templeton, Reynolds averaged turbulence modelling using deep neural networks with embedded invariance, J. Fluid Mech. **807**, 155 (2016).

[8] S. B. Pope, A more general effective-viscosity hypothesis, J. Fluid Mech. **72**, 331 (1975).

[9] N. Geneva and N. Zabaras, Quantifying model form uncertainty in Reynolds-averaged turbulence models with Bayesian deep neural networks, J. Comput. Phys. **383**, 125 (2019).

[10] J. Weatheritt and R. Sandberg, A novel evolutionary algorithm applied to algebraic modifications of the RANS stress–strain relationship, J. Comput. Phys. **325**, 22 (2016).

[11] M. Schmelzer, R. P. Dwight, and P. Cinnella, Discovery of algebraic Reynolds-stress models using sparse symbolic regression, Flow Turbul. Combust. **104**, 579 (2020).

[12] H. Tang, Y. Wang, T. Wang, and L. Tian, Discovering explicit Reynolds-averaged turbulence closures for turbulent separated flows through deep learning-based symbolic regression with non-linear corrections, Phys. Fluids **35**, 025118 (2023).

[13] L. Zhu, W. Zhang, J. Kou, and Y. Liu, Machine learning methods for turbulence modeling in subsonic flows around airfoils, Phys. Fluids **31**, 015105 (2019).

[14] Y. Liu, W. Cao, W. Zhang, and Z. Xia, Analysis on numerical stability and convergence of Reynolds averaged Navier–Stokes simulations from the perspective of coupling modes, Phys. Fluids **34**, 015120 (2022).

[15] A. P. Singh and K. Duraisamy, Using field inversion to quantify functional errors in turbulence closures, Phys. Fluids **28**, 045110 (2016).

[16] M. B. Giles, M. C. Duta, J.-D. Muller, and N. A. Pierce, Algorithm developments for discrete adjoint methods, AIAA J. **41**, 198 (2003).

[17] A. P. Singh, S. Medida, and K. Duraisamy, Machine-learning-augmented predictive modeling of turbulent separated flows over airfoils, AIAA J. **55**, 2215 (2017).

[18] C. Yan, Y. Zhang, and H. Chen, Data augmented turbulence modeling for three-dimensional separation flows, Phys. Fluids **34**, 075101 (2022).

[19] C. Wu and Y. Zhang, Enhancing the shear-stress-transport turbulence model with symbolic regression: A generalizable and interpretable data-driven approach, Phys. Rev. Fluids **8**, 084604 (2023).

[20] G. Evensen, The ensemble Kalman filter: Theoretical formulation and practical implementation, Ocean Dyn. **53**, 343 (2003).

[21] M. A. Iglesias, K. J. H. Law, and A. M. Stuart, The ensemble Kalman filter for inverse problems, Inverse Probl. **29**, 045001 (2013).

[22] X.-L. Zhang, H. Xiao, X. Luo, and G. He, Ensemble Kalman method for learning turbulence models from indirect observation data, J. Fluid Mech. **949**, A26 (2022).

[23] M. A. Iglesias, A regularizing iterative ensemble Kalman method for PDE-constrained inverse problems, Inverse Probl. **32**, 025002 (2016).

[24] M. Hanke, A regularizing Levenberg-Marquardt scheme, with applications to inverse groundwater filtration problems, Inverse Probl. **13**, 79 (1997).

[25] X. Luo, A. S. Stordal, R. J. Lorentzen, and G. Nævdal, Iterative ensemble smoother as an approximate solution to a regularized minimum-average-cost problem: Theory and applications, SPE J. **20**, 962 (2015).

[26] X.-L. Zhang, C. Michelén-Ströfer, and H. Xiao, Regularized ensemble Kalman methods for inverse problems, J. Comput. Phys. **416**, 109517 (2020).

[27] M. Yang and Z. Xiao, Improving the $k$–$\omega$–$\gamma$–$A_r$ transition model by the field inversion and machine learning framework, Phys. Fluids **32**, 064101 (2020).

[28] T.-X. Zhang, J.-Q. Chen, F.-Z. Zeng, D.-G. Tang, and C. Yan, Improvement of transition prediction model in hypersonic boundary layer based on field inversion and machine learning framework, Phys. Fluids **35**, 024104 (2023).

[29] J. Wu, H. Xiao, R. Sun, and Q. Wang, Reynolds-averaged Navier-Stokes equations with explicit data-driven Reynolds stress closure can be ill-conditioned, J. Fluid Mech. **869**, 553 (2019).

[30] H. Tang, Y. Wang, T. Wang, L. Tian, and Y. Qian, Data-driven Reynolds-averaged turbulence modeling with generalizable non-linear correction and uncertainty quantification using Bayesian deep learning, Phys. Fluids **35**, 055119 (2023).

[31] Y. Zhao, H. D. Akolekar, J. Weatheritt, V. Michelassi, and R. D. Sandberg, RANS turbulence model development using CFD-driven machine learning, J. Comput. Phys. **411**, 109413 (2020).

[32] Z. Wang and W. Zhang, A unified method of data assimilation and turbulence modeling for separated flows at high Reynolds numbers, Phys. Fluids **35**, 025124 (2023).

[33] D. J. S. Aulakh, X. Yang, and R. Maulik, Robust experimental data assimilation for the Spalart-Allmaras turbulence model, Phys. Rev. Fluids **9**, 084608 (2024).

[34] H. Jasak, A. Jemcov, and Z. Tukovic, OpenFOAM: A C++ library for complex physics simulations, in *International Workshop on Coupled Methods in Numerical Dynamics* (University of Zagreb, Croatia, 2007), pp. 1–20.

[35] P. E. Smirnov and F. R. Menter, Sensitization of the SST turbulence model to rotation and curvature by applying the Spalart–Shur correction term, J. Turbomach. Trans. ASME **131**, 041010 (2009).

[36] T. P. Dhakal and D. K. Walters, A three-equation variant of the SST $k$-$\omega$ model sensitized to rotation and curvature effects, J. Fluids Eng. **133**, 111201 (2011).

[37] A. Hellsten, Some improvements in Menter's k-Omega SST turbulence model, in *29th AIAA Fluid Dynamics Conference, Albuquerque, NM, USA* (AIAA, Reston, VA, 1998), p. 2554.

[38] Y. Zhang, X. Wang, Y. Zhang, and C. Liu, Comparisons and analyses of vortex identification between Omega method and Q criterion, J. Hydrodyn. **31**, 224 (2019).

[39] W. Kobayashi, T. Shimura, A. Mitsuishi, K. Iwamoto, and A. Murata, Prediction of the drag reduction effect of pulsating pipe flow based on machine learning, Int. J. Heat Fluid Flow **88**, 108783 (2021).

[40] Z. Mao, A. D. Jagtap, and G. E. Karniadakis, Physics-informed neural networks for high-speed flows, Comput. Methods Appl. Mech. Eng. **360**, 112789 (2020).

[41] J.-Z. Peng, Z.-Q. Wang, X. Rong, M. Mei, M. Wang, Y. He, and W.-T. Wu, Rapid and sparse reconstruction of high-speed steady-state and transient compressible flow fields using physics-informed graph neural networks, Phys. Fluids **36**, 046113 (2024).

[42] R. D. Sanhueza, S. H. H. J. Smit, J. W. R. Peeters, and R. Pecnik, Machine learning for RANS turbulence modeling of variable property flows, Comput. Fluids **255**, 105835 (2023).

[43] M. Abadi *et al.*, TensorFlow: Large-scale machine learning on heterogeneous distributed systems, arXiv:1603.04467.

[44] P. L. Houtekamer and H. L. Mitchell, A sequential ensemble Kalman filter for atmospheric data assimilation, Mon. Weather Rev. **129**, 123 (2001).

[45] C. H. Bishop, B. J. Etherton, and S. J. Majumdar, Adaptive sampling with the ensemble transform Kalman filter. Part I: Theoretical aspects, Mon. Weather Rev. **129**, 420 (2001).

[46] N. B. Kovachki and A. M. Stuart, Ensemble Kalman inversion: A derivative-free technique for machine learning tasks, Inverse Probl. **35**, 095005 (2019).

[47] X. Luo, Ensemble-based kernel learning for a class of data assimilation problems with imperfect forward simulators, PLoS One **14**, e0219247 (2019).

[48] C. A. M. Ströfer, X.-L. Zhang, and H. Ciao, DAFI: An open-source framework for ensemble-based data assimilation and field inversion, arXiv:2012.02651.

[49] H. Xiao, J.-L. Wu, S. Laizet, and L. Duan, Flows over periodic hills of parameterized geometries: A dataset for data-driven turbulence modeling from direct simulations, Comput. Fluids **200**, 104431 (2020).

[50] H. Le, P. Moin, and J. Kim, Direct numerical simulation of turbulent flow over a backward-facing step, J. Fluid Mech. **330**, 349 (1997).

[51] S. Jovic and D. M. Driver, Backward-facing step measurements at low Reynolds number, Reh = 5000, NASA Memorandum No. 108807 (1994).

[52] R. Matai and P. Durbin, Large-eddy simulation of turbulent flow over a parametric set of bumps, J. Fluid Mech. **866**, 503 (2019).

[53] R. McConkey, E. Yee, and F.-S. Lien, A curated dataset for data-driven turbulence modeling, Sci. Data **8**, 255 (2021).

[54] D. M. Somers, Design and Experimental Results for the S805 Airfoil, Report No. NREL/SR-440-6917, National Renewable Energy Laboratory, Golden, CO (1997).

[55] D. M. Somers, Design and Experimental Results for the S809 Airfoil, Report No. NREL/SR-440-6918, National Renewable Energy Laboratory, Golden, CO (1997).

[56] D. M. Somers, Design and Experimental Results for the S814 Airfoil, Report No. NREL/SR-440-6919, National Renewable Energy Laboratory, Golden, CO (1997).